

DIFFUSION-CONTROLLED KINETIC EVOLUTION OF RADIATION-INDUCED  
POINT DEFECTS IN POLYCRYSTALLINE  $\text{UO}_2$  FROM ATOMIC-LEVEL SIMULATION

By

KUN-TA TSAI

A THESIS PRESENTED TO THE GRADUATE SCHOOL  
OF THE UNIVERSITY OF FLORIDA IN PARTIAL FULFILLMENT  
OF THE REQUIREMENTS FOR THE DEGREE OF MASTER OF SCIENCE

UNIVERSITY OF FLORIDA

2010

© 2010 Kun-Ta Tsai

To my family with love and gratitude

## ACKNOWLEDGEMENTS

First of all, I would like to express my sincerest gratitude to my advisor Prof. Simon R. Phillpot for his invaluable guidance and encouragement. In the beginning, for me as a non-native speaker of English, the Santa Claus' British accent distances us. Nonetheless, throughout my master's study, I am subtly but deeply influenced by his wisdom and enthusiasm towards science blended with a great sense of humor. He likes to share his knowledge by throwing open questions and to give us the liberty to brainstorm. It is my greatest honor to have him as my advisor. I would also like to express my deepest appreciation to my committee members Prof. Susan B. Sinnott and Prof. Juan C. Nino for providing valuable suggestions to my research work.

I feel extremely fortunate to work with a wonderful team, the Computational Materials Science Focus Group. I want to specially thank Dr. Dilpuneet Aidhy for his kind help on my research work. This thesis benefited immensely and would not be accomplished without him. I am also thankful to Dr. Tao Liang, Dr. Alex Chernatinsky, Dr. Rakesh Behera, Dr. Haixuan Xu, Mr. Donghwa Lee, Mr. Priyank Shukla, Mr. Chan-woo Lee, Mr. Donghyun Kim, and Mr. Eric Bucholz for their friendly assistance. I want to mention my two dearest senior friends Tze-Ray Shan and Yu-Ting Cheng. Many thanks to both of them for constant support and encouragement in my life inside and outside the school.

Finally, I would like to thank my family for continuous support with unconditional love. This thesis is dedicated to them.

## TABLE OF CONTENTS

	<u>page</u>
ACKNOWLEDGEMENTS .....	4
LIST OF TABLES.....	7
LIST OF FIGURES.....	8
ABSTRACT .....	10
CHAPTER	
1 INTRODUCTION .....	12
1.1 Sources of Energy .....	12
1.2 Nuclear Energy .....	14
1.3 Radioactive Decay and Nuclear Fission .....	18
1.4 Motivation and Objective .....	22
1.5 Beauty of Simulation .....	23
2 DEFECTS IN SOLIDS .....	24
2.1 Introduction .....	24
2.2 Intrinsic Point Defects .....	24
2.2.1 Schottky Defect.....	25
2.2.2 Frenkel Defect .....	25
2.2.3 Thermodynamics of Point Defects: Equilibrium Concentration .....	26
2.3 Grain Boundary.....	27
2.4 Atom Movements in Materials.....	28
2.4.1 Diffusion Mechanisms.....	28
2.4.2 Atomic Theory of Diffusion.....	30
2.5 Crystallography of UO <sub>2</sub> .....	34
2.6 Radiation Damage .....	36
3 SIMULATION METHODOLOGY.....	39
3.1 Simulation Methodologies.....	39
3.2 Molecular Dynamics Simulation.....	41
3.3 General MD Algorithm .....	41
3.4 Periodic Boundary Condition .....	43
3.5 Interatomic Interactions .....	44
3.5.1 Long-Range Interactions.....	45
3.5.2 Short-Range Interactions.....	46
3.5.3 Thermodynamic Conditions (Ensembles) for Simulations.....	47
3.5.4 Thermostat.....	49
3.5.5 Barostat .....	49
3.6 Conventional Radiation Damage Method by MD Simulations.....	50

4	GRAIN BOUNDARY INFLUENCE ON RADIATION DAMAGE IN $UO_2$ .....	52
4.1	Kinetically-Evolving Irradiation-Induced Defects Method by MD Simulation .....	52
4.2	Simulation Methodology .....	52
4.2.1	MD Simulation .....	52
4.2.2	Defects Analysis Methods.....	54
4.3	Results.....	56
4.3.1	Frenkel-Pair Defects in Single-Crystal $UO_2$ .....	56
4.3.2	Frenkel-Pair Defects in Polycrystalline $UO_2$ .....	58
4.3.3	Grain Boundary Source/Sink Behaviors for Point Defects .....	63
4.3.4	Vacancy Clustering: V-4O Clusters .....	77
4.3.5	Vacancy Clustering: Schottky Defects .....	74
4.3.6	Interstitial Clustering: Cuboctahedral Clusters .....	75
5	CONCLUSIONS AND FUTURE WORK .....	79
5.1	Conclusions .....	79
5.2	Future Work.....	82
	LIST OF REFERENCES .....	83
	BIOGRAPHICAL SKETCH.....	88

## LIST OF TABLES

<u>Table</u>	<u>page</u>
3-1 Potential parameters used in the present work.....	48

## LIST OF FIGURES

<u>Figure</u>	<u>page</u>
1-1	1973 and 2007 fuel shares of total primary energy supply ..... 12
1-2	Evolution from 1971 to 2007 of world total primary energy supply by fuel ..... 13
1-3	World net nuclear electric power generation (1980-2006) ..... 16
1-4	World map for commercial nuclear power plants ..... 17
2-1	Point defects: (a) vacancy, and (b) interstitial ..... 25
2-2	Point defects in (a) Schottky defect, and (b) Frenkel defect ..... 26
2-3	Schematic representation of three diffusion mechanisms..... 29
2-4	Fluorite crystal structure. .... 35
2-5	Three different symmetry operations for the fluorite crystal structure ..... 36
2-6	Defect evolution during ballistic and kinetic phases of the radiation damage .... 37
3-1	Hierarchical multi-scale approach to computational material engineering. .... 40
3-2	Periodic boundary conditions of a fluorite structure supercell..... 44
3-3	Inter-ionic potential as a function of distance between U <sup>+2.4</sup> and O <sup>-1.2</sup> ions... 48
4-1	Fully equilibrated polycrystalline UO <sub>2</sub> microstructure. .... 53
4-2	Schematic representations of the common neighbor analysis (CNA) ..... 54
4-3	Schematic representations of the lattice matching analysis (LMA)..... 55
4-4	Evolution of O FPs in the single crystal. .... 57
4-5	Snapshot of evolution of point defect in polycrystal ..... 62
4-6	Evolution of O FPs in the polycrystal ..... 63
4-7	Snapshots showing the GB being the source for the O vacancy ..... 65
4-8	Close-up views of the GB being the source for the O vacancy. .... 66
4-9	Progressive snapshots showing the GB being the sink for the O vacancy ..... 67
4-10	Close-up views of the GB being the sink for the O vacancy ..... 68

4-11	Single point alignment offsets.....	69
4-12	Snapshots showing the GB being the sink for the O interstitial .....	71
4-13	Close-up views of the GB being the sink for the O interstitial .....	72
4-14	Three different configurations of Schottky defects.....	74
4-15	Snapshot showing Schottky defects .....	75
4-16	Formation process of COT clusters.....	76
4-17	Snapshot showing COT clusters .....	77
4-18	Configurations of V-4O clusters.....	78
4-19	Snapshot showing V-4O oxygen clusters.....	78

Abstract of Thesis Presented to the Graduate School  
of the University of Florida in Partial Fulfillment of the  
Requirements for the Degree of Master of Science

DIFFUSION-CONTROLLED KINETIC EVOLUTION OF RADIATION-INDUCED  
POINT DEFECTS IN POLYCRYSTALLINE  $\text{UO}_2$  FROM ATOMIC-LEVEL SIMULATION

By

Kun-Ta Tsai

August 2010

Chair: Simon R. Phillpot  
Major: Materials Science and Engineering

Nuclear energy is capable of providing people with energy for some billions of years if used properly. In most operating nuclear reactors, fluorite-structured  $\text{UO}_2$  is used as the fuel. After irradiation,  $\text{UO}_2$  undergoes structural damage by forming high concentration of point defects, which can limit the lifetime of the fuel. In order to enhance the radiation tolerance of  $\text{UO}_2$ , it is of great interest to understand the fundamental mechanism of intrinsic point defects evolution under different conditions.

Rather than a single crystal, this thesis focuses on the more representative polycrystalline  $\text{UO}_2$ , and uses molecular dynamics (MD) as the modeling tool. This study provides a better understanding of defects evolution in the kinetic phase at the atomistic scale.

In addition to spontaneous vacancy-interstitial recombination events, some of the point defects are found to have interactions with GBs. These source/sink behaviors take place by a set of interstitialcy diffusion processes. The diffusion direction is ascertained to follow the primary diffusion direction  $\langle 001 \rangle$  for the fluorite-based structure with the reasonable oxygen vacancy diffusivity on the order of  $10^{-6} \text{ cm}^2/\text{s}$  ( $10^{-4} \text{ \AA}^2/\text{s}$ ). A mean

square displacement calculation confirms that atoms may realign after the diffusion activity, supporting the concept that damage can be healed by GBs in a macroscopic sense.

It is also found that the presence of defects on the U sub-lattice can lead to the formation of clusters, which make  $\text{UO}_2$  less radiation tolerant. In addition, the equilibrium concentration of O defects is much larger in polycrystal than that in single crystal. This can be attributed to GBs possibly supplying O defects into the bulk.

# CHAPTER 1 INTRODUCTION

## 1.1 Sources of Energy

“Energy can be neither created nor destroyed,” say our science books, “but can only be transferred from one form to another.” Mankind has been engaged with this transformation since life began on the planet. Since industrialization, humans have utilized a variety of energies and explored more. With growth accelerating in developing countries, demands on energy resources are being stretching to new limits. In recent decades, the urgent need for energy has created a global movement to exploit all potential materials. On the other hand, materials are used to produce energy or enable energy to be converted into other useful forms. Energy and materials therefore have a continual and mutually enriching relationship.

The choice of materials for energy generation depends on the availability and accessibility of the source. Fig. 1-1 gives pie charts of the fraction of the total primary

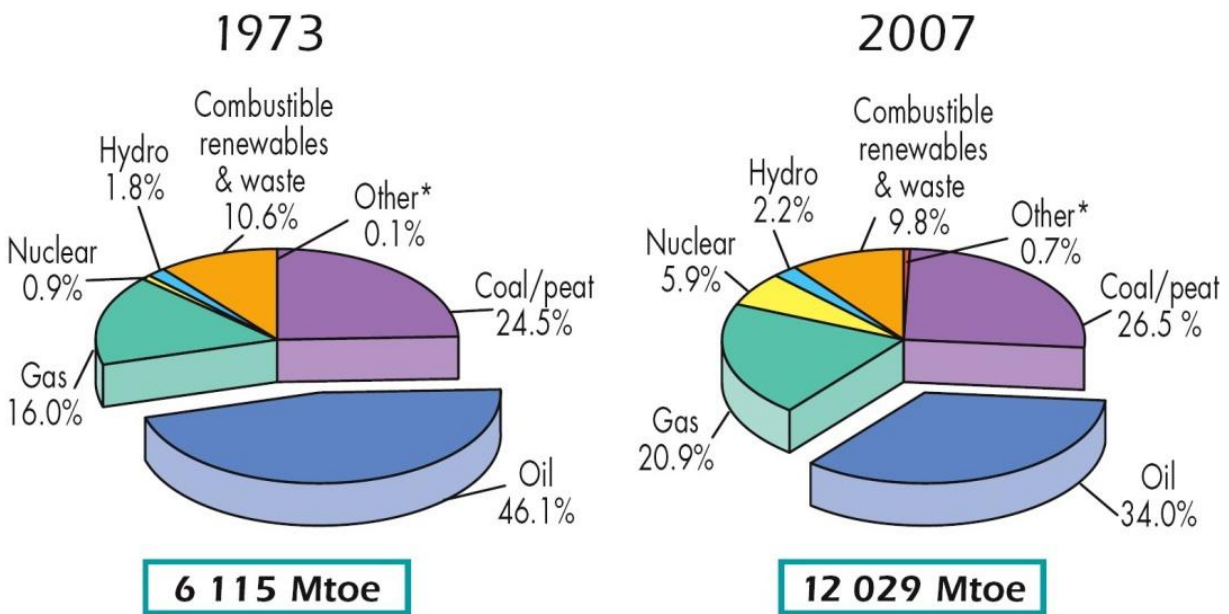


Figure 1-1. 1973 and 2007 fuel shares of total primary energy supply (Mtoe, million tonne of oil equivalent). (\*Others include geothermal, solar, wind, heat, etc.)<sup>1</sup>

energy from various sources supply in 1973 and 2007.<sup>1</sup> It was estimated by the International Energy Agency (IEA) that in 2007 primary sources of energy consisted of oil 34.0 %, coal/peat 26.5 %, and natural gas 20.9 %, amounting to an 81.4 % share of fossil fuels in primary energy consumption in the world. This indicates the world's significant dependence on fossil fuels due to their continuing widespread availability and the large developed infrastructure. Yet fossil fuels are non-renewable resources and their production raises many environmental concerns; thus there has been a gradual movement towards cleaner fuels. Fig. 1-2 shows the evolution from 1971 to 2007 of world total primary energy supply by fuel.<sup>1</sup> It should be noted that hydro power was surpassed by nuclear power in total electrical generation in 1984, and that nuclear the share has increased to 5 % of the total energy supply over the last 34 years. Along with increasing awareness of environmental issues, nuclear energy is expected to play an important role in the energy portfolio in the coming decades.<sup>2</sup>

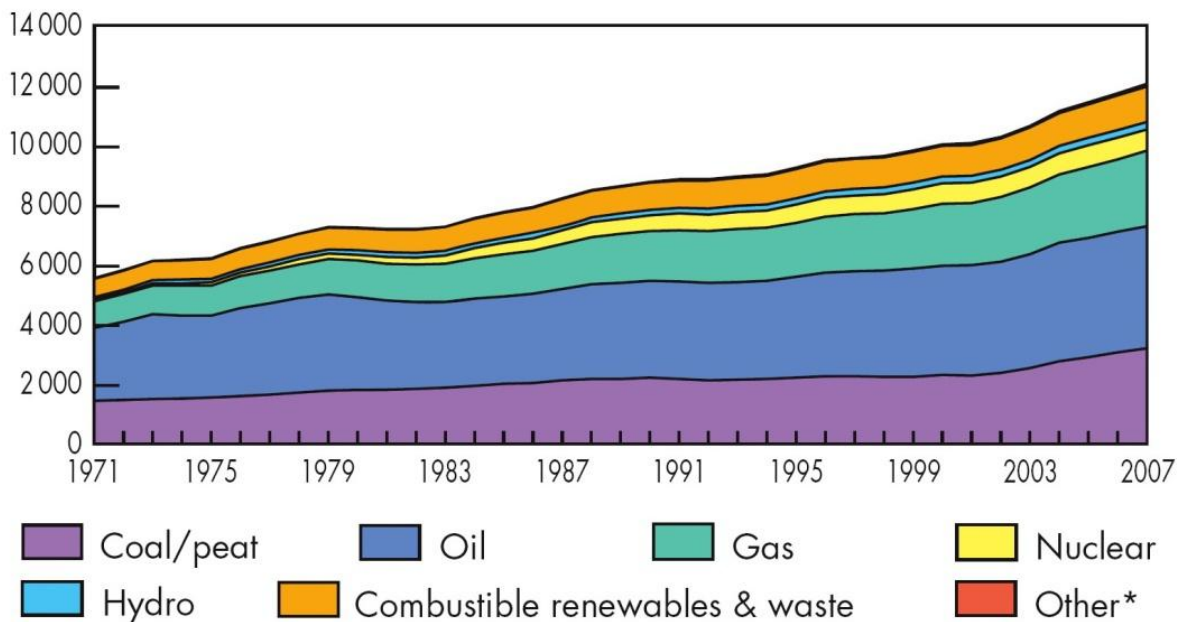


Figure 1-2. Evolution from 1971 to 2007 of world total primary energy supply by fuel (Mtoe).<sup>1</sup>

## 1.2 Nuclear Energy

Ernest Rutherford is one of the central figures in the exploration of nuclear physics. He was awarded the 1908 Nobel Prize in Chemistry for investigations into the disintegration of the elements and the chemistry of radioactive substances.<sup>3</sup> “. . . *Taking the atomic weight of the emanation as 222, one gram of the emanation emits during its life  $2 \times 10^9$  gram calories of heat. This evolution of heat is enormous compared with that emitted in any known chemical reaction. . .*”, excerpted from Rutherford’s article in *Encyclopedia Britannica* (1910).<sup>4</sup> The basic energy fact is that the fission of a uranium atom generates 10 million times the energy as that produced by burning an atom of carbon from coal. This concept that a large amount of energy can be released by the disintegration of an atom was soon brought to public attention.

The first time that electricity was generated by a nuclear reactor occurred in an Idaho experimental station.<sup>5</sup> The world’s first nuclear power plant was operational in Russia in 1954 generating around 5 megawatts (MW) of electric power.<sup>6</sup> In the following years, other nuclear stations were opened in the U.S. and the U.K., etc. In the early years, nuclear capacity increased rapidly, rising from less than 1 gigawatt (GW) in 1960 to 100 GW in the late 1970s, and 300 GW in the late 1980s.<sup>7</sup> Since then, the increase in worldwide capacity started to slow down due to consecutive major nuclear accidents in Three Mile Island (1979) and Chernobyl (1986). More and more anti-nuclear movements arose based on the fear of possible nuclear disasters, radiation, and waste production. Despite those controversies, many countries remain active in developing nuclear power, including China, India, Japan, and Republic of Korea.<sup>8</sup> With modern designs to meet strict safety standards, nuclear reactors are becoming much more reliable. In addition, the superiority of the non-CO<sub>2</sub>-emitting source makes nuclear energy more promising.

Nuclear power energy can be generated by two types of nuclear reactions: fission and fusion. Fission-based nuclear technology is well established, whereas fusion technology is expected to become commercially available in the second half of the century. The most widely used material for fission is uranium. Natural uranium is almost entirely composed of two isotopes, U-238 (99.3 %) and U-235 (0.7 %), indicating that U-238 is about 140 times more prevalent than U-235. However, only U-235 can directly sustain the fission chain reaction as a nuclear fuel source; U-238 is not fissionable with thermal neutrons.

A nuclear power reactor has a large number of fuel rods in the core. Every rod contains pellets of uranium oxide. When an atom of U-235 is hit by a neutron, it can undergo a fission reaction, producing two fission fragments and other free neutrons with a very high speed. In steady-state operation of the reactor, the free neutron is absorbed by another U-235 atom leading to another fission. The kinetic energy of other fission products is converted to thermal energy when they are stopped by nearby atoms. The heat then is absorbed by water, which becomes steam to drive the turbines to generate the electricity. The power level of the reactor can be controlled by the amount of steam withdrawn. In addition, the control rods which absorb neutrons can also be moved in and out of the reactor to avoid the reactor temperature getting too high.

Some analysts suggest that oil wells might be depleted within 70-80 years.<sup>9</sup> Natural gas might run out a little later. Yet present reactors that use only the U-235 in natural uranium will likely have fuel supplies for some hundreds of years. Bernard Cohen, a Newton scholar in history of science, even predicts that with breeder reactors, we can have plenty of energy for some billions of years.<sup>10</sup>

If more efficient usage of neutrons in the reactor is designed, U-238 could be converted to plutonium, which produces more fissionable materials. This kind of design is called a breeder reactor.<sup>7</sup> Thus, with the usage of U-238 as the fuel in breeder reactors, fuel resources based on breeder reactors could provide adequate energy for billions of years. Commercial breeder reactors have been deployed in several countries, such as the U.S., U.K., France, Russia, Japan, and India.<sup>11</sup> Breeder reactors can be regarded as a kind of resource instead of just a reserve. Because their cost is a lot higher than present reactors, and because large uranium reserves have also been discovered in recent years, it is perhaps unlikely that we will see breeder reactors all over the world soon. Nevertheless, in the very long term, breeder reactors will be used since they supply about 100 times as much energy from a kilogram of uranium as do present reactors. This will make the present stock of uranium go much farther.

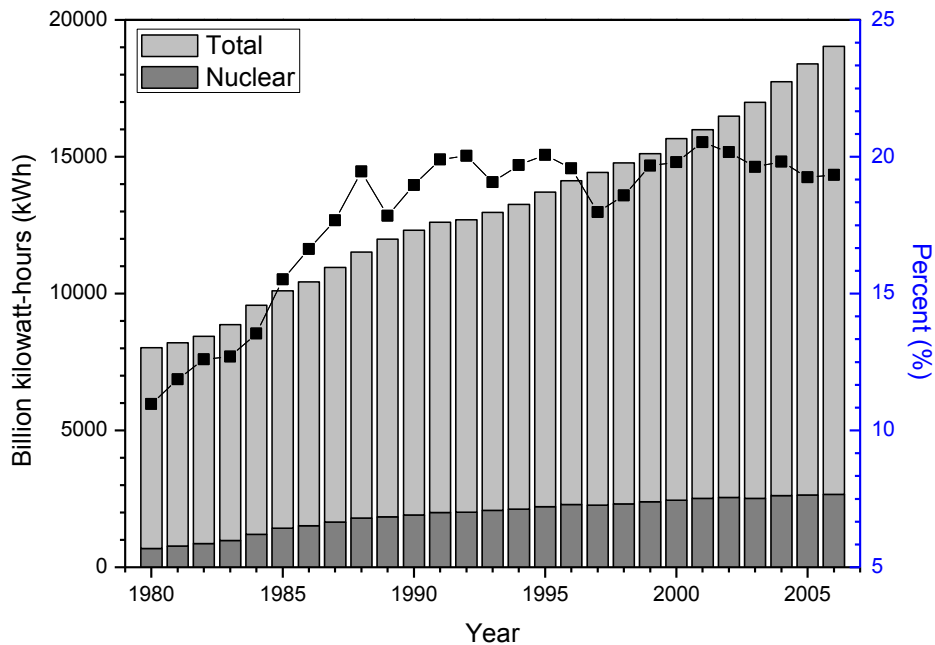


Figure1-3. World net nuclear electric power generation (1980-2006).<sup>12</sup>

Fig. 1-3 demonstrates the world net nuclear electric power generation from 1980 to 2006. The nuclear share of electricity net generation increased from 4.5 % in 1973 to around 20 % in 1990, since then it has been approximately constant.<sup>12</sup> According to International Atomic Energy Agency (IAEA), there are 436 commercial nuclear power plants, operating in 31 countries, as illustrated in Fig. 1-4.<sup>13</sup> Not all the world is employing nuclear energy. France generates 78 % of its electricity from nuclear reactors, most of the rest being hydroelectric. Japan is close to 30 % and increasing steadily due to their lack of domestic coal and oil.<sup>14</sup> Ten African countries are now in pursuit of their own nuclear plants because wind and solar solutions are not reliable enough.

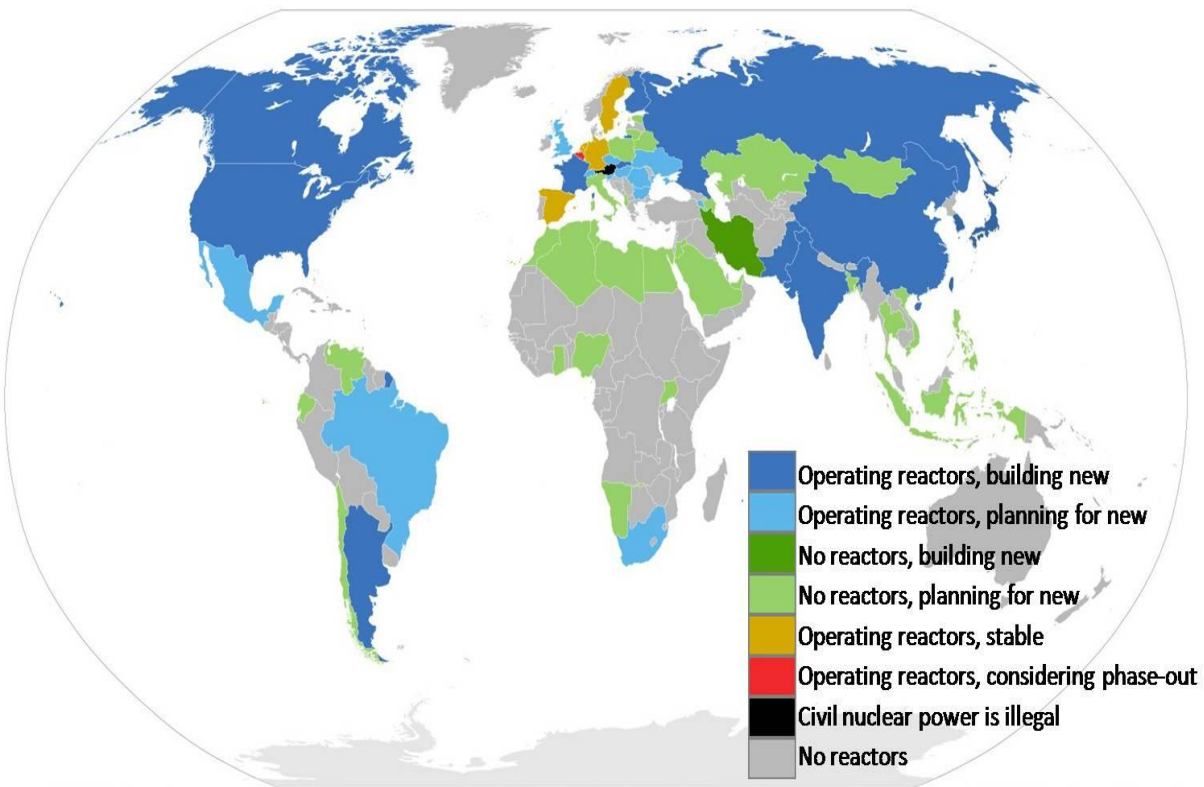


Figure1-4. World map for commercial nuclear power plants (research reactors not included).<sup>13</sup>

To sum up, in the short term, probably the next hundred years, there is so much uranium that no one can profitably prospect for more. In the medium term, breeder

reactors will extend the energy obtained per kilogram of uranium by a factor of about 100. In the very long term, plenty of uranium can be extracted from seawater for a few billion years.

After being no longer efficient in sustaining a nuclear reaction in the nuclear reactor (usually at the nuclear power plant), spent nuclear fuel is put in storage condition. Spent nuclear fuel is highly radioactive and potentially very harmful, such as causing incapacitation and death. The radioactivity of nuclear wastes decreases with the passage of time through radioactive decay. For radioactive materials, the amount of time needed to decrease the radioactivity to one-half the original amount is called the radioactive half-life.<sup>15</sup> Many of the radioactive elements in spent fuel have long-lives. For example, U-235 has the half-life of 713,000,000 years, and U-238 has the half-life of 4500,000,000 years.<sup>16</sup> With these long-lived radioactive elements, nuclear fuel must be isolated and controlled for thousands of years by a barrier or radiation protection shield. Department of Energy (DOE) is developing plans for a permanent disposal facility for spent fuel at Yucca Mountain and Nevada.<sup>15</sup> This has aroused some controversy, particularly with state and local authorities. Several complementary measures are still required for the long-term development of nuclear energy.

### **1.3 Radioactive Decay and Nuclear Fission**

Spontaneous radioactivity was first recognized by a French physicist, Henri Becquerel, in 1896 while investigating phosphorescence in uranium salt. Along with Marie Curie and Pierre Curie, who jointly found another two radioactive elements, radium and polonium in 1898, they won the 1903 Noble Prize in Physics.<sup>17</sup>

The main processes of radioactivity involve four types of decay; alpha (  $\alpha$  ) decay, beta (  $\beta$  ) decay, gamma (  $\gamma$  ) decay, and neutron capture.

**Alpha ( $\alpha$ ) decay:** Alpha decay is the process in which a nucleus ejects an alpha particle, which is essentially the helium-4 nucleus ( ${}^4_2\text{He}^{+2}$ ). For example, Eq. 1-1<sup>18</sup> represents the daughter nucleus ( ${}^{234}_{90}\text{Th}$ ) emitted by the parent atom ( ${}^{238}_{92}\text{U}$ ), producing an alpha particle.



Alpha decay is the most common type of nuclear decay for elements with atomic number greater than 82. This is because the greatest bonding energy is lost per nucleon and the alpha particle is an especially low energy arrangement of two protons and two neutrons. The typical kinetic energy of alpha particles is about 5 MeV with a speed of 15,000 km/s (i.e. 5% of the speed of light). Being relatively slow, heavy, and positively charged, alpha particles have a short free path in length that is so small that they easily interact with other atoms by losing their kinetic energy within a very short distance, usually a few centimeters of air. Therefore, external alpha radiation is generally not harmful.

**Beta ( $\beta$ ) decay:** Beta decay is the transformation of a proton into a neutron with emission of a positron, or the transformation of a neutron into a proton with emission of an electron. It occurs when there are too many protons or neutrons in a nucleus.<sup>19</sup> There are three kinds of beta decay, beta plus ( $\beta^+$ ) decay, beta minus ( $\beta^-$ ) decay, and electron capture (*K*-capture).

In  $\beta^+$  decay, the weak nuclear force converts a proton into a neutron while emitting a positron ( $e^+$ ) and an electron neutrino ( $\nu_e$ ):



Neutrinos are electrically neutral elementary particles that travel at the speed of light.

In  $\beta^-$  decay, a neutron transforms into a proton by emitting an electron ( $e^-$ ) and an electron antineutrino ( $\bar{\nu}_e$ ):



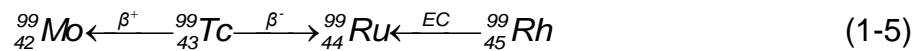
Antineutrinos are antiparticles of neutrinos.

The third type of beta decay is electron capture, which is where  $\beta^+$  decay accompanies a shell electron throughout the decay process. It can be expressed as:



This decay is also called *K*-capture because the innermost electron lies in the *K*-shell, which has the highest probability to interact with the nucleus.

To sum up, within all types of beta decay, the atomic number of the parent nucleus is different from that of the daughter nucleus while the mass number is the same. All three general types of beta decay of  ${}_{43}^{99}\text{Tc}^{20}$  and  ${}_{45}^{99}\text{Rh}^{21}$  are represented in Eq. 1-5:



The kinetic energy of beta particles depends on the parent and daughter nuclear states in the decay chain, typically ranging from a few keV to a few tens of MeV. The most energetic beta particles can reach speeds approaching the speed of light. In addition, because they are less charged and much smaller than alpha particles, beta particles generally travel further into tissues, which can cause cells damage at the molecular level.

**Gamma ( $\gamma$ ) decay:** Gamma decay refers to as a nucleus jumping down from a higher energy state to a lower one by emitting electromagnetic radiation (photons), which is known for the gamma ray:



There is no change in the number of protons and neutrons between the parent and daughter nuclei throughout the process, but the emitted gamma rays are characteristic for each decay. Gamma rays typically have energies in the range from 100k keV to 10 MeV and wavelength less than 10 pm, which is often smaller than an atom. Therefore, they are usually more penetrating, and can cause biological damage.

**Neutron capture:** Neutrons are electrically neutral, so more easily interact with a nucleus than charged particles. In neutron capture, a nucleus collides with a neutron to merge into a heavier one with a higher energy state.<sup>22</sup> The excited nucleus quickly decays to the ground state through emission of gamma rays:



In this type of decay, the mass number rises by one, which is crucial for the formation of heavier elements in the cosmos. Nuclei with mass numbers greater than 56 can be created by neutron capture but are unlikely to be formed by thermonuclear reactions (i.e. nuclear fusion).

**Nuclear fission:** Nuclear fission is a form of nuclear transmutation in which an atom is induced to split into two lighter elements with emission of free neutrons:



In the event, two more new neutrons are produced, which make the reaction be a self-sustaining chain reaction in the nuclear reactor. The energy released by the fission fragments and neutrons can be roughly approximated from the mass differences<sup>21</sup>:

$$Q = [m({}^{235}\text{U}) - m({}^{144}\text{Ba}) - m({}^{89}\text{Kr}) - 2m_n]c^2 = 173\text{MeV} \quad (1-10)$$

This simple calculation is very close to real results (180.5 MeV), including the kinetic

energy of the fission fragments (168.2 MeV) and the neutrons (4.8 MeV), as well as the energy carried off by gamma rays (7.5 MeV). Taking into account other contributions by following decay reactions, the sum of above process gives an average total energy of 195 MeV.<sup>23</sup> Compared with this high energy, a typical chemical reaction usually only involves energy changes less than 10 eV.

#### 1.4 Motivation and Objective

This thesis focuses on nuclear materials, especially on understanding the fundamental mechanism of intrinsic point defects evolution, which plays a crucial role in the material performance. In nuclear reactors, the uranium dioxide ( $\text{UO}_2$ ) fuel undergoes structural damage (formation of defects) after irradiation. Radiation damage (RD) due to high concentration of point defects can limit the lifetime of the fuel. In order to enhance the radiation tolerance of  $\text{UO}_2$ , it is of great interest to accurately predict the long term behavior under different conditions.

Real nuclear fuels are made of several  $\text{UO}_2$  crystals separated by interfaces or grain boundaries (GBs). To determine the GB effect, the results obtained in a single crystal are generally used to compare with those in polycrystalline materials. Therefore, building on the previous work by Aidhy *et al.* in single-crystal  $\text{UO}_2$ <sup>24</sup>, this thesis investigates more realistic polycrystalline  $\text{UO}_2$ . It has been justified that defect evolution is largely independent of the initial damage state on MgO simulations.<sup>25</sup> Therefore, conventional molecular dynamics (MD) simulations using primary knock-on atom (PKA) approach are not capable of capturing the long-term evolution of point defects, mainly due to lack of complete development of complex defect structures. Moreover, in order to elucidate the interplay of U and O point defects, evolution from initially different defect conditions has to be studied. This is also not possible for standard MD using PKA

approach. As a result, a new methodology is developed to perform such atomic simulation to characterize detailed physical processes associated with GBs and to indicate to what extent GBs interact with the defects.

### **1.5 Beauty of Simulation**

Although  $\text{UO}_2$  has been extensively studied in the past, there is little understanding of its microscopic behavior during irradiation. This is because experiments are expensive and have little access to the defect length scale and irradiation events time scale. In a nuclear reactor, radiation events occur on a very short time scale (~nanoseconds), so observing them by experiment is not possible. Hence, atomic simulation can be a complementing alternative to obtain valuable information and widen the scope of knowledge in this area.

Understanding the basic diffusion mechanism at the atomic scale is a key ingredient in the development of realistic macroscopic models. Moreover, GBs in polycrystalline materials are known to largely influence these events, which take place simultaneously with vacancy-interstitial recombination in the bulk. Only simulations are able to directly distinguish the process and to determine the dominant mechanism. On the other hand, it is also not experimentally possible to capture a material's responses to the presence of different types of point defects, which might reveal its ability to maintain the desired properties.

## CHAPTER 2 DEFECTS IN SOLIDS

### 2.1 Introduction

The scientific study of crystalline solids is better developed than that of amorphous materials due to their regularity and symmetry. On the atomic scale, crystalline solids are composed of a set of atoms arranged in a particular way with repeating pattern throughout all three spatial dimensions. There are a large number of crystal structures, from the simple ones of elemental metals to complex ceramics. It is impossible to maintain the infinite long-range order in all three dimensions. In general, the regularity is often disrupted by defects. These imperfections may have a profound effect on the properties of materials. Defects can be classified into three categories by their dimensions: three-dimensional bulk defects (e.g. voids or precipitates), two-dimensional planar defects (e.g. grain boundaries or interfaces), one-dimensional line defects (e.g. dislocations), and zero-dimensional point defects (e.g. vacancies or interstitials). In this work, the behavior of point defects is of our focus.

### 2.2 Intrinsic Point Defects

From the Nernst theorem it is known that a crystal may have a perfect structure only at the absolute zero temperature.<sup>26</sup> Therefore, a small number of intrinsic point defects are always present at any temperature above absolute zero. Imperfections involving atoms only native to the crystal without any external intervention (e.g. Na or Cl in NaCl crystals) are called “intrinsic” defects. They do not require the introduction of impurities or aliovalent ions and are intrinsically related to the structure of the compound. The vacancy is simply an atom missing from a lattice site, which would be occupied in a perfect lattice as in Fig. 2-1 (a). The self-interstitial is an atom crowded in a void space

between lattice atoms as in Fig. 2-1 (b). These point defects in the lattice create varying separations between the neighboring atoms, which hence generate lattice strains.

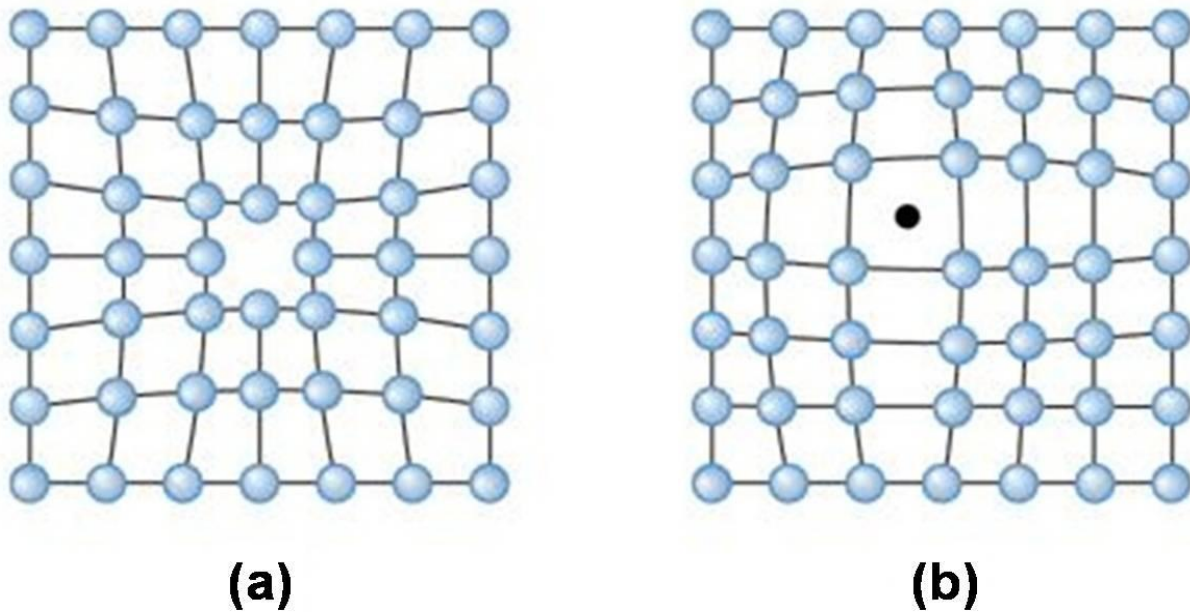


Figure 2-1. Point defects: (a) vacancy, and (b) interstitial.<sup>27</sup>

### 2.2.1 Schottky Defect

A Schottky defect is unique to ionic materials and is commonly found in ceramics. It forms when stoichiometric numbers of ions are missing from the crystal lattice, leaving behind vacancies on the cation and anion sites in order to maintain overall electrical neutrality in the material, as shown in Fig. 2-2 (a). The defect is named after the German Scientist Walter H. Schottky. The following is the chemical reaction in Kröger-Vink notation for the formation of the Schottky defect in  $\text{UO}_2$ :



### 2.2.2 Frenkel Defect

In crystals containing more than one ion, vacancies and interstitials may occupy either anion or cation sites. A Frenkel defect (or Frenkel pair (FP)) is a vacancy-interstitial

pair created by thermal vibration when an ion hops from a normal lattice site to a nearby interstitial site, leaving behind a vacancy. It was named after the Russian scientist Yakov Frenkel, who discovered the phenomenon in 1926.<sup>28</sup> Fig. 2-2 (b) is a schematic representation of a Frenkel defect for an ionic material. Frenkel defects can also be found in metals and covalent compounds.

Taking oxides as an example, the Frenkel defect on the oxygen anion sub-lattice site can be described using Kröger-Vink notation as:

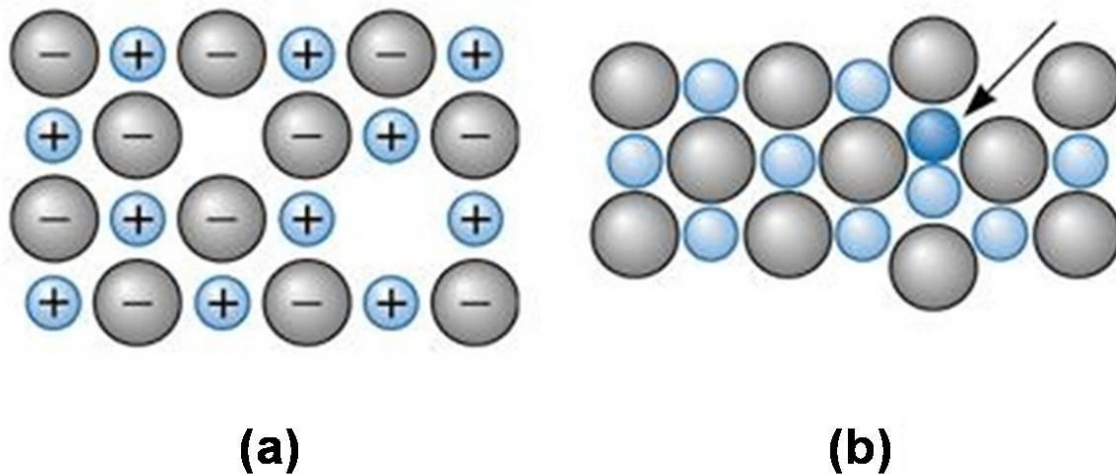


Figure 2-2. Point defects in (a) Schottky defect, and (b) Frenkel defect.<sup>27</sup>

There are also other types of point defects, both intrinsic and extrinsic. However, only Frenkel defects are under study in this thesis.

### 2.2.3 Thermodynamics of Point Defects: Equilibrium Concentration

The formation of intrinsic point defects is governed by the principle of minimizing the total Gibbs free energy. Any destruction of the perfect lattice may increase the lattice energy. However, when point defects are present, the overall randomness or entropy of

the material increases, and hence can decrease the total Gibbs free energy, which can increase the thermodynamic stability of a crystalline material. Vacancies play an important role in determining the rate at which atoms or ions can move around, or diffuse in a solid material, especially in pure metals.

At room temperature, the concentration of point defects is small, but the equilibrium numbers of point defects  $n_v$  and  $n_i$  increases exponentially as the temperature is increased, as shown by the following Arrhenius equations:<sup>29</sup>

$$n_v = N \cdot \exp\left(\frac{-Q_v}{kT}\right) \quad (2-3)$$

$$n_i = N \cdot \exp\left(\frac{-Q_i}{kT}\right) \quad (2-4)$$

where  $n_v$  and  $n_i$  are the number of vacancies and interstitials per  $\text{cm}^3$ ;  $N$  is the number of atoms per  $\text{cm}^3$ ;  $Q_v$  and  $Q_i$  are the energy required to produce a vacancy and interstitial, in eV/mol;  $k$  is the Boltzmann constant,  $8.617 \times 10^{-5}$  eV/K;  $T$  is the temperature in Kelvin.

### 2.3 Grain Boundary

Grain boundaries (GBs) are the lattice defects which have been longest known but least understood. Most engineering materials are polycrystalline in nature in that they are made of many single crystals which are misoriented with respect to each other. In a polycrystalline solid, GBs are the internal interfaces that separate neighboring regions of the same crystal structure but of different orientation. These interfaces, which are usually planar, have a two-dimensional periodic atomic structure. For example, considering grains in 100 diameter in a polycrystalline cube with 1 cm on edge, there would be more than  $10^{15}$  grains, with a GB area of several square meters. Thus, the details of the atomic structures of GBs play an important role in controlling the properties of the polycrystalline

solid. According to the misorientation between adjacent grains, low-angle grain boundaries (LAGBs) are those with a slight orientation mismatch, which can be described in terms of dislocation arrays.<sup>29</sup> For high-angle grain boundaries (HAGBs), the properties are normally independent of the misorientation angle. The transition angle varies from 10-20 degrees, but is not known exactly.<sup>30</sup> Tilt boundaries are formed when angle of misorientation lies in the plane of boundaries, which can be described by an array of edge dislocations. When the angle of misorientation is parallel to the plane of boundaries, twist boundaries result, which can be described by means of screw dislocation arrays. Symmetric boundaries bisect the angle of rotation. A twin boundary is a special type of GB in a mirror-symmetric manner. In general, GBs have very different atomic configurations and local atomic densities from those of the perfect crystal. The deficiency of fundamental knowledge of GBs is mainly due to their complex structure, which requires extensive description for their macroscopic characterization.

## 2.4 Atom Movements in Materials

### 2.4.1 Diffusion Mechanisms

Understanding of diffusion is based on two important fundamentals<sup>31</sup>: (1) the continuum theory of diffusion originated from work of the German scientist Adolf Fick, and (2) the Brownian motion detected by the Scottish botanist Robert Brown.

**Vacancy diffusion:** As mentioned in 2.2.3, in thermodynamic equilibrium at elevated temperature, a specific number of vacancies are present in a crystal. Vacancy diffusion involves the movement of an atom from a regular lattice position into an adjacent vacant lattice site; thus the atom and the vacancy move in opposite directions (Fig. 2-3 (a)). The number of vacancies, which increases as the temperature increases, determines the extent of this mode of diffusion.

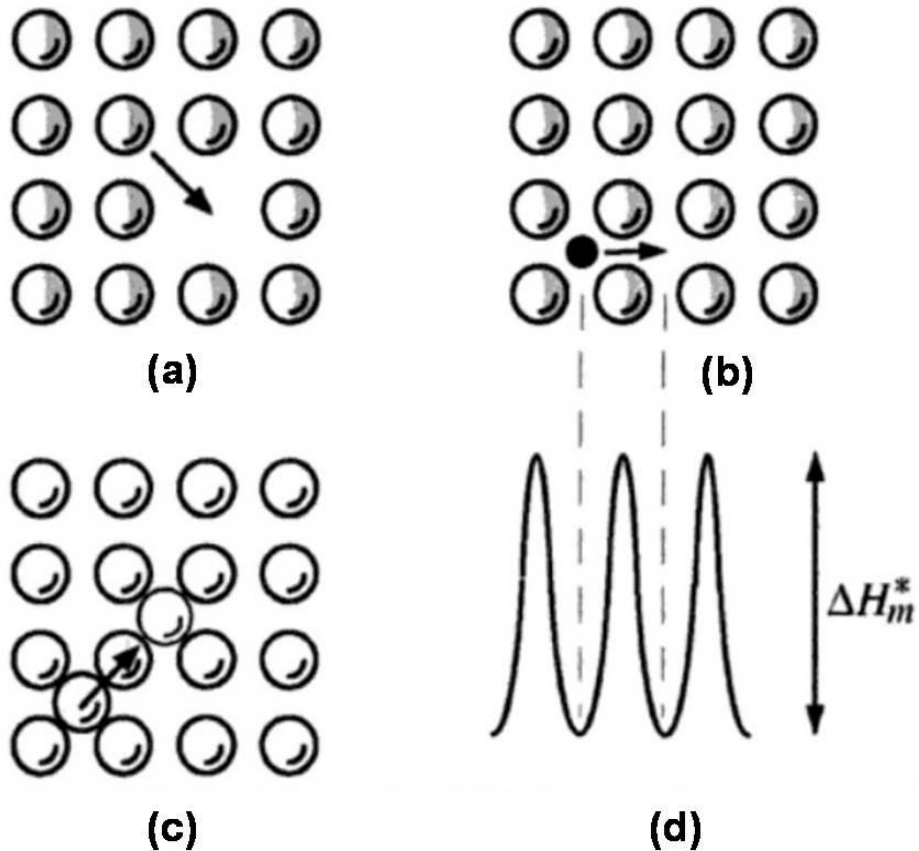


Figure 2-3. Schematic representation of three diffusion mechanisms: (a) vacancy diffusion mechanism, (b) interstitial diffusion mechanism, (c) interstitialcy mechanism, and (d) enthalpy barrier  $\Delta H_m^*$  required to make a jump for the interstitial atom shown in (b).<sup>32</sup>

**Interstitial diffusion:** This type of diffusion involves an interstitial atom directly migrating to another nearby interstitial site without causing the net motion of any other atom (Fig. 2-3 (b)).

In some modes, to make the jump, an enthalpy barrier has to be overcome for the atom to squeeze through a narrow passage. This enthalpy barrier is known for the migration energy and is shown schematically in Fig. 2-3 (d).

The migration energy of the vacancy is larger than that of the interstitial, so the pre-exponential diffusivity of the vacancy is much smaller. There are two main reasons why interstitial diffusion takes place much faster than diffusion by vacancy mode.<sup>29</sup> First,

interstitial atoms are usually smaller and thus more mobile. Second, there are more interstitial positions than vacant sites, so the probability of interstitial atomic movement is greater than vacancy diffusion.

**Interstitialcy diffusion:** A less common mechanism is the interstitialcy mechanism, where an interstitial atom pushes an atom into an interstitial site and move into the lattice site itself (Fig. 2-3 (c)). This mechanism of diffusion will be observed in this research.

#### 2.4.2 Atomic Theory of Diffusion

**Phenomenological equations:** Diffusion is the phenomenon of material transport by atomic motion.<sup>29</sup> In solids, diffusion is a very slow process. The rate at which atoms diffuse in a material can be measured by the flux ( $J$ ), defined as the number of atoms passing through a cross-sectional unit area per unit time. If the diffusion is steady-state in one dimension ( $x$ -direction), which means flux does not change with time, the net flux of atoms can be described by Fick's first law:

$$J_x = -D \frac{dc}{dx} \quad (2-5)$$

where  $D$  is the self-diffusion coefficient, which is a measure of the ease and frequency with which that atom jumps around in a crystal lattice in the absence of external forces, i.e., in a totally random fashion. Experimentally, the temperature dependence of the diffusivity is:

$$D = D_0 \cdot \exp\left(-\frac{\Delta H_m^*}{RT}\right) \quad (2-6)$$

where  $\Delta H_m^*$  is the enthalpy barrier for diffusion independent of temperature;  $D_0$  is a temperature-independent pre-exponential parameter. Note that the diffusion rate largely decreases with decreasing temperature.

**Atomistics of solid state diffusion:** In general, diffusion in solids occurs in the presence of point defects.<sup>33</sup> Ion irradiation results in the formation of vacancy-interstitial pairs.<sup>34</sup> If the defects are produced at temperatures where they are mobile, they can partly anneal out by diffusion. Therefore, the balance between the formation rate and the annihilation rate leads to a steady state of the excess concentration of defects. Atoms usually move by interchanging positions between atoms and neighboring vacant sites. For such a diffusion process, the relationship relating the diffusion coefficient (  $D$  ) of an atom to the diffusion jump distance (  $\lambda$  ) in a solid is:<sup>32</sup>

$$D = \alpha \Omega \lambda^2 \quad (2-7)$$

where  $\alpha$  is a geometric constant depending on the crystal structure, and  $\Omega$  is the frequency of successful jumps.

The jump frequency is the product of the probability of an atom having sufficient energy to make a jump (  $\nu$  ) and the probability of available adjacent vacant sites (  $\theta$  ):

$$\Omega = \nu \theta \quad (2-8)$$

where  $\nu$  can be further expressed by:

$$\nu = \nu_0 \cdot \exp\left(-\frac{\Delta H_m^*}{k_B T}\right) \quad (2-9)$$

where  $\Delta H_m^*$  is the enthalpy barrier required to make a jump, and  $\nu_0$  is vibrational frequency of the atom.

**Defect diffusivity:** As noted previously, the two major defects responsible for the movement of atoms are vacancies and interstitials. For both cases at low concentrations, the sites adjacent to the defect will be always available, so  $\theta \approx 1$ .<sup>33</sup>

An interstitial will make a jump with the rate only depending on its frequency of

successful jumps. By combining Eq. (2-7), (2-8), and (2-9), the interstitial diffusivity  $D_i$  is given by:

$$D_i = \alpha_i \lambda^2 v_0 \cdot \exp\left(-\frac{\Delta H_m^*}{k_B T}\right) \quad (2-10)$$

On the other hand, for a vacancy, the probability of successful jumps is increased  $\zeta$ -fold, where  $\zeta$  is the coordination number of the vacancy. Thus, the vacancy diffusivity  $D_v$  is expressed by:

$$D_v = \alpha \zeta \lambda^2 v_0 \cdot \exp\left(-\frac{\Delta H_m^*}{k_B T}\right) \quad (2-11)$$

**Atom diffusivity:** In contrast to the vacancies and interstitials, most atoms have few available sites nearby into which they can diffuse, so  $\theta \ll 1$ .<sup>32</sup> The probability of a site being vacant is simply equal to the vacancy fraction in the solid, denoted by  $\Lambda$ . Therefore, the atomic diffusivity  $D_A$  is given by the following expression, which resembles Eq. (2-6), namely:

$$D_A = \alpha \zeta \lambda^2 \Lambda v_0 \cdot \exp\left(-\frac{\Delta H_m^*}{k_B T}\right) = D_0 \cdot \exp\left(-\frac{\Delta H_m^*}{k_B T}\right) \quad (2-12)$$

Comparing Eq. (2-11) and (2-12) reveals an important relationship between vacancy and atom diffusivity:

$$D_A = \Lambda D_v \quad (2-13)$$

We assume that  $\Lambda \approx f_v \cdot c_v / c_A \ll 1$ , where  $f_v$  is a correlation factor, and  $c_A$ ,  $c_v$  are the concentrations of atoms and vacancies, respectively. A more useful expression is thus given by:<sup>34</sup>

$$D_A c_A = f_v D_v c_v \quad \text{or} \quad D_A c_A = f_i D_i c_i \quad (2-14)$$

Correlation factors depend on the crystal structure and diffusion mechanism. The

theoretical values for fluorite structures have been reported for the three mechanisms: 0.653 for the free vacancy, 1 for the interstitial, and 0.739 for the indirect non-collinear interstitialcy.<sup>35</sup> The physical picture of Eq. (2-14) is easy to grasp: the defects (vacancies or interstitials) move often (high  $D$ ) but are not that numerous, while the atoms move less frequently (low  $D$ ) but are much more in number.

With  $c_A \approx 1$ , rearranging Eq. (2-14) yields:

$$D_v = \frac{D_A}{c_v f_v} \quad (2-15)$$

$$D_i = \frac{D_A}{c_i f_i} \quad (2-16)$$

**Diffusivity in simulations:** In atomic simulations, the self-diffusivity is determined based on the time evolution of the mean square displacement (MSD) under zero-stress conditions. The quantity can be easily calculated by recording the atomic positions during the simulation:

$$MSD(t) = \frac{1}{N} \sum_{i=1}^N [\vec{r}_i - \vec{r}_0]^2 = \langle |\vec{r}_i - \vec{r}_0|^2 \rangle \quad (2-17)$$

where  $N$  is the total number of ions;  $t$  is the simulation time;  $\vec{r}_i$  and  $\vec{r}_0$  are atomic positions at time =  $t$  and  $0$ , respectively; the angular brackets here denote an average over the square of the displacement that the atom has undergone during a time interval  $t$ . Since the thermal energy is involved in the MSD, atomic positions can be simply related with the initial thermal velocity  $\vec{v}_i(0)$ :

$$\vec{r}_i(t) = \vec{r}_i(0) + \vec{v}_i(0)t \quad (2-18)$$

Inserting Eq. (2-18) into (2-17) gives:

$$\langle |\bar{r}_i - \bar{r}_0|^2 \rangle = \frac{1}{N} \sum_{i=1}^N [\bar{v}_i(0)]^2 t^2 \quad (2-19)$$

From kinetic-molecular theory, the average kinetic energy is proportional to the absolute temperature in the following relation:

$$\frac{1}{2} m v_{rms}^2 = \frac{3}{2} k_B T \quad (2-20)$$

where  $v_{rms}$  is the root mean square velocity. Inserting Eq. (2-20) into (2-19) gives:

$$\langle |\bar{r}_i - \bar{r}_0|^2 \rangle = v_{rms}^2 t^2 = \frac{3k_B T}{m} t^2 \quad (2-21)$$

For liquids, the MSD grows linearly with time, while for solids, the MSD saturates to a finite value. It is useful to characterize the diffusive motion in terms of the slope, which is the self-diffusion coefficient of the atoms ( $D_A$ ), namely:

$$\langle |\bar{r}_i - \bar{r}_0|^2 \rangle \sim 6D_A t$$

$$D_A = \frac{1}{6t} \langle |\bar{r}_i - \bar{r}_0|^2 \rangle \quad (2-22)$$

## 2.5 Crystallography of $\text{UO}_2$

In this thesis, the central theme is on the evolution of point defects in the fluorite-based  $\text{UO}_2$ . As shown in Fig. 2-4, the fluorite structure can be viewed as a face-centered cubic (FCC) array of cations, represented by blue spheres, with the anions residing in all the tetrahedral sites, represented by red spheres.

A fluorite crystal unit cell consists of four U atoms and eight O atoms. The coordination number of the cation is eight and that of the anion is four. The cations occupy the Wyckoff site  $4a$  and the anions occupy  $8b$ . The space group of fluorite crystal is  $Fm\bar{3}m$  (number 225 and point group symmetry  $m\bar{3}m$ <sup>36</sup>).  $Fm\bar{3}m$  can be fully written

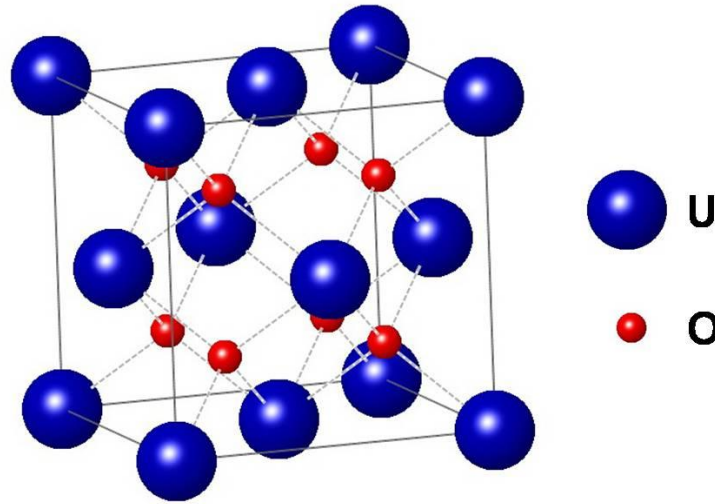


Figure 2-4. Fluorite crystal structure. The FCC network of cations (blue spheres) with anions (red spheres) occupying the tetrahedral sites.

as  $F\frac{4}{m}\bar{3}\frac{2}{m}$ . The first letter refers to the lattice type. Here,  $F$  stands for face-center cubic

(FCC). The following three sets of symbols denote the three kinds of symmetry directions of the lattice relative to the space group, naming primary, secondary, and tertiary

directions, respectively. For the FCC unit cell, the primary symmetry directions are  $\langle 100 \rangle$ , i.e.,  $[100]$ ,  $[010]$ , and  $[001]$ ; the secondary symmetry directions are  $\langle 111 \rangle$ ; the tertiary symmetry directions are  $\langle 110 \rangle$ .

In the  $F\frac{4}{m}\bar{3}\frac{2}{m}$  symmetry,  $\frac{4}{m}$  represents four-fold rotational symmetry along the principle axis with a mirror plane perpendicular to the axis.  $\bar{3}$  refers to the rotoinversion along the diagonal (i.e. secondary) direction of the unit cell.  $\frac{2}{m}$  stands for two-fold rotation along the edge of the unit cell (i.e. tertiary direction) with a mirror plane perpendicular to the edge. Fig. 2-5 schematically shows all three symmetry operations mentioned above.

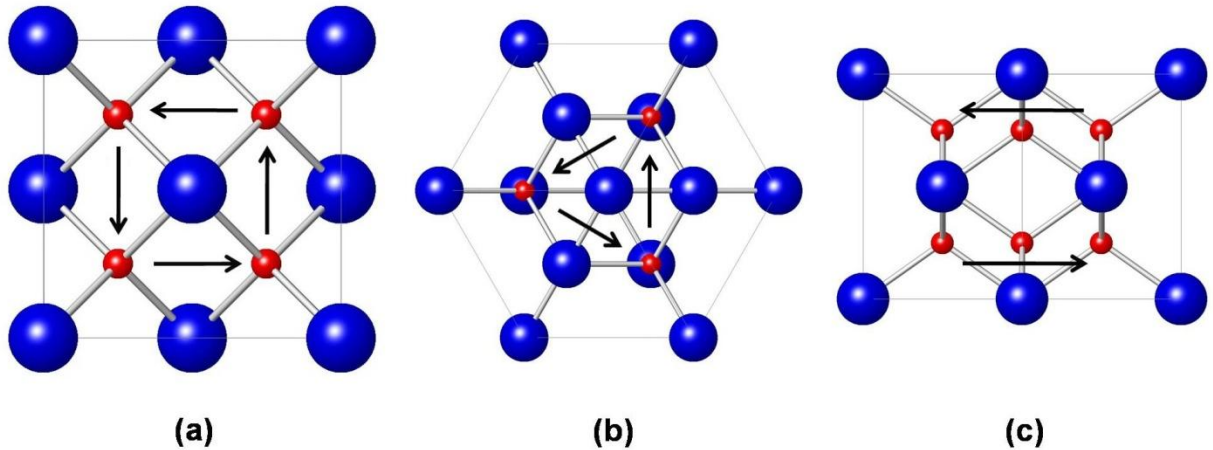


Figure 2-5. Graphic representation of three different symmetry operations for space group  $F\frac{4}{m}\frac{3}{m}\frac{2}{m}$ : (a) four-fold rotation along  $\langle 100 \rangle$ , (b) three-fold rotation along  $\langle 111 \rangle$ , and (c) two-fold rotation along  $\langle 110 \rangle$ .

## 2.6 Radiation Damage

Nuclear energy is part of solution to the increasing global energy demand and concerns about greenhouse gas emissions. A fundamental understanding of defect formation, accumulation, and annihilation in irradiated ceramics is required to develop novel radiation tolerant ceramics for improving the performance of the fuel, and for developing long-lasting storage materials.

When materials are bombarded with radiation, electrons may come out of their original orbitals, and atoms may displace from their original sites. In this process, defects are also introduced, either by bombarding ions residing in the material or following nuclear reactions. Therefore, the properties of the material are altered, sometimes heavily, sometimes just slightly. These spontaneous processes can lead to the gradual and ultimately complete amorphization of the ceramic crystalline structure, which is undesirable for nuclear application because it is often accompanied by degradation of thermo-mechanical properties and reduced chemical durability. However, sometimes

defects can be annealed out, so the material will remain crystalline. The radiation response of ceramics relies on a dynamic balance between damage by defect accumulation and recovery from thermal annealing.

The radiation damage phenomena take place in a very short time, and include two important phases (Fig. 2-6).<sup>37</sup> The “ballistic phase” involves the atomic collision cascade arising from the high-energy “primary knock-on atom” (PKA). Atoms are displaced from their original lattice sites, thereby producing a large number of point defects and small clusters. The “ballistic phase” usually lasts only a few picoseconds. By contrast, the “kinetic phase” lasts longer, and captures the mainly time-dependent diffusion-controlled kinetic evolution of these defects, including the annihilation and formation of larger long-lasting defect clusters. Some defects may recombine or be eliminated at microstructural sinks (GBs, dislocations, or external surface); others cluster to form voids or interstitial loops. Annihilation of point defects promotes radiation tolerance of the

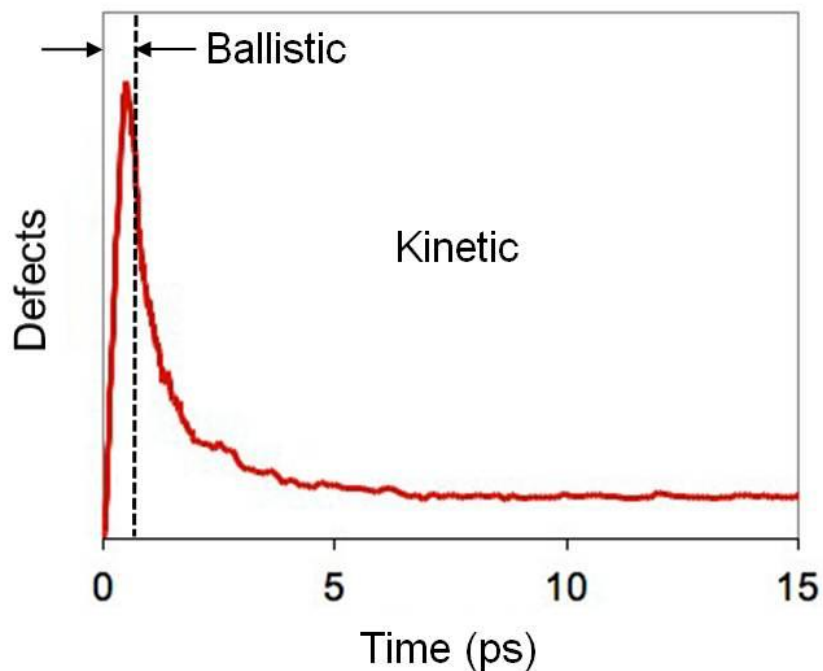


Figure 2-6. Defect evolution during ballistic and kinetic phases of the radiation damage.<sup>37</sup>

material while clusters lead to long-lived radiation damage. As a result, the “kinetic phase” process determines the performance and lifetime of the material. Understanding the defect evolution during the “kinetic phase” is thus crucial for engineering radiation tolerant ceramics, and in  $\text{UO}_2$  it is also the central problem of this thesis.

## CHAPTER 3 SIMULATION METHODOLOGY

Computer simulations are carried out to solve material science problems related to the design a material with specified properties and functionalities. They have high potential to impact real industrial research and development. As a matter of fact, simulations serve as a complement to conventional experiments, enabling us to integrate computational and theoretical methods with experimental analysis and characterization methods.

### 3.1 Simulation Methodologies

To characterize various materials behaviors over wide length and time scales, a wide set of simulation methodologies are used, as show in Fig. 3-1.

Starting at the highest level, engineering design is basically the primary analytical tool for relatively large-scale manufacturing systems in industry, varying from integrated circuits to distillation columns and engines. At the level of continuum models, gradual transitions without abrupt changes or discontinuities are described, such as macroscopic stresses, large temperature gradients. Below this level, the meso-scale modeling includes kinetic Monte Carlo (KMC) models<sup>38</sup> and phase-field methods<sup>39</sup> as approaches to modeling and predicting morphological and microstructure evolution. A further level down, atomic phenomena are accurately captured by molecular dynamics (MD) simulation with interatomic potentials<sup>40</sup> and force fields<sup>41</sup>. Details of this method will be discussed in the following section. At the lowest level, computational quantum chemical methods are characterized by quantum mechanics at the level of the electronic structure. Electronic states are described in terms of the Schrödinger equation:<sup>42</sup>

$$H\Psi = E\Psi \quad (3-1)$$

where  $E$  is the total system energy (eigenvalue);  $H$  is the Hamiltonian operator;  $\Psi$  is the wave function (eigenfunction). There are two main approximation methods to solve the equation: semi-empirical methods and *ab initio* methods. Semi-empirical methods use experimentally derived parameters to strive for accuracy, but *ab initio* methods use calculations to evaluate all integrals. With correlation, *ab initio* methods can even have accuracy comparable with experiments in structure and energy predictions. However, calculations become extremely demanding in computer resources.

This work focuses on phenomena at the atomistic length scale and picosecond time scale; therefore, MD simulation is chosen here.

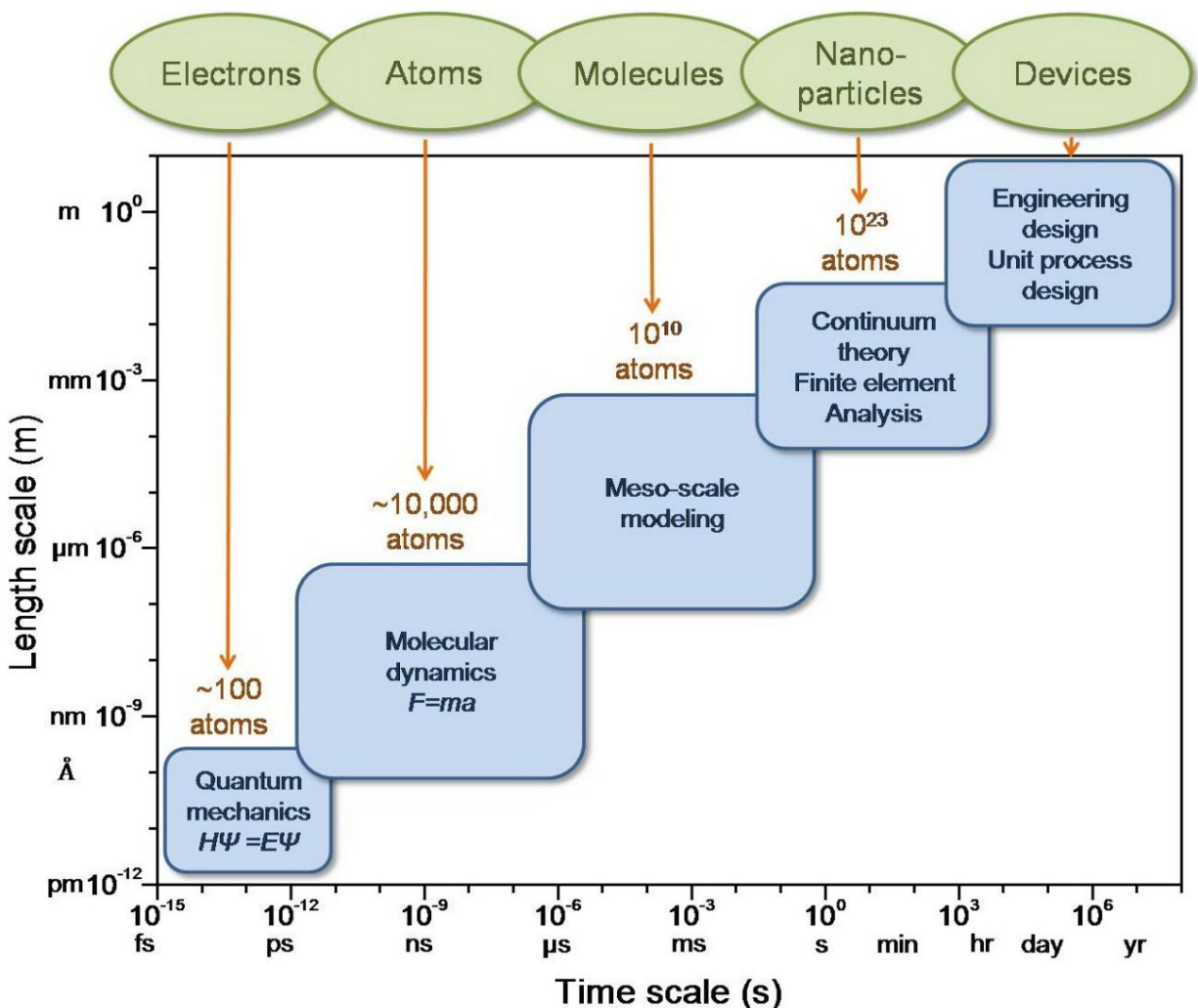


Figure 3-1. Hierarchical multi-scale approach to computational material engineering.

### 3.2 Molecular Dynamics Simulation

The MD simulation is a technique that computes time-dependent behaviors, such as structures, dynamics, and thermodynamics. It enables us to probe features of the motion of atoms, and to take “still snapshots” of crystal structures. Now it is frequently used in the study of materials science because no conventional experiment allows access to all the time scale of motion with the atomic resolution. The accuracy of the calculated properties relies entirely on the fidelity of the interatomic potential, which is typically defined by quantum based methods or experimental data.

### 3.3 General MD Algorithm

In MD simulations, all atoms are given initial positions theoretically, which is defined by the crystal structure of the material and the microstructure of interest. The atoms are assigned random velocities ( $v$ ) according to the simulation temperature ( $T$ ):

$$\frac{1}{2}mv^2 = \frac{3}{2}k_B T \quad (3-2)$$

where  $m$  is the mass of the atom;  $k_B$  is the Boltzmann's constant.

The motion of the atom can be described by solving Newton's second law:

$$\vec{F} = m\vec{a} = m \frac{d^2 \vec{r}}{dt^2} \quad (3-3)$$

where  $F$  is force exerted in the atom;  $m$  is its mass;  $\vec{a}$  is its acceleration. The force can also be calculated from the gradient of the interatomic potential energy  $V$ :

$$\vec{F} = -\nabla V \quad (3-4)$$

Numerous numerical algorithms have been developed for integrating the equations of motion, such as Verlet<sup>43</sup>, leap-frog<sup>44,45</sup>, Beeman's<sup>46</sup>, and predictor-corrector<sup>47</sup>. They differ in accuracy and computational load. In this thesis, a fifth-order Gear predictor-

corrector method is used. This method consists of three steps: prediction, evaluation, and correction.

In the first prediction step, a high-order Taylor expansion is performed to estimate the atom positions around time  $t$  to predict the positions at  $t+\Delta t$ :

$$\begin{aligned}\bar{r}^p(t+\Delta t) &= \bar{r}(t) + \frac{d\bar{r}(t)}{dt} \Delta t + \frac{1}{2} \frac{d^2\bar{r}(t)}{dt^2} (\Delta t)^2 + \frac{1}{3!} \frac{d^3\bar{r}(t)}{dt^3} (\Delta t)^3 + \frac{1}{4!} \frac{d^4\bar{r}(t)}{dt^4} (\Delta t)^4 + \frac{1}{5!} \frac{d^5\bar{r}(t)}{dt^5} (\Delta t)^5 \\ \bar{v}^p(t+\Delta t) &= \frac{d\bar{r}(t)}{dt} + \frac{d^2\bar{r}(t)}{dt^2} \Delta t + \frac{1}{2} \frac{d^3\bar{r}(t)}{dt^3} (\Delta t)^2 + \frac{1}{3!} \frac{d^4\bar{r}(t)}{dt^4} (\Delta t)^3 + \frac{1}{4!} \frac{d^5\bar{r}(t)}{dt^5} (\Delta t)^4 \\ \bar{a}^p(t+\Delta t) &= \frac{d^2\bar{r}(t)}{dt^2} + \frac{d^3\bar{r}(t)}{dt^3} \Delta t + \frac{1}{2} \frac{d^4\bar{r}(t)}{dt^4} (\Delta t)^2 + \frac{1}{3!} \frac{d^5\bar{r}(t)}{dt^5} (\Delta t)^3 \\ \bar{b}^p(t+\Delta t) &= \frac{d^3\bar{r}(t)}{dt^3} + \frac{d^4\bar{r}(t)}{dt^4} \Delta t + \frac{1}{2} \frac{d^5\bar{r}(t)}{dt^5} (\Delta t)^2 \\ \bar{c}^p(t+\Delta t) &= \frac{d^4\bar{r}(t)}{dt^4} + \frac{d^5\bar{r}(t)}{dt^5} \Delta t \\ \bar{d}^p(t+\Delta t) &= \frac{d^5\bar{r}(t)}{dt^5}\end{aligned}\tag{3-5}$$

The superscript refers to predicted values;  $\bar{r}$ ,  $\bar{v}$ ,  $\bar{a}$ ,  $\bar{b}$ ,  $\bar{c}$  and  $\bar{d}$  denotes positions, velocities, accelerations, and third, fourth, and fifth time derivative of position, respectively.

Newton's second law is introduced. Therefore, the correct accelerations can be obtained:

$$\bar{a}^c = \frac{\bar{F}}{m} = -\frac{1}{m} \frac{d\bar{V}(r^p)}{dr}\tag{3-6}$$

where  $F$  is the force exerted on the atom;  $m$  is its mass;  $a$  is its acceleration. The acceleration can be evaluated by comparing with the predicted accelerations from Eq.

(3-5), to estimate the error in the prediction step:

$$\Delta\bar{a}(t + \Delta t) = \Delta\bar{a}^c(t + \Delta t) - \Delta\bar{a}^p(t + \Delta t) \quad (3-7)$$

This error and the results of the prediction step are fed into the correction step:

$$\begin{aligned} \bar{r}^c(t + \Delta t) &= \bar{r}^p(t + \Delta t) - c_0 \Delta\bar{a}(t + \Delta t) \\ \bar{v}^c(t + \Delta t) &= \bar{v}^p(t + \Delta t) - c_1 \Delta\bar{a}(t + \Delta t) \\ \bar{a}^c(t + \Delta t) &= \bar{a}^p(t + \Delta t) - c_2 \Delta\bar{a}(t + \Delta t) \\ \bar{b}^c(t + \Delta t) &= \bar{b}^p(t + \Delta t) - c_3 \Delta\bar{a}(t + \Delta t) \\ \bar{c}^c(t + \Delta t) &= \bar{c}^p(t + \Delta t) - c_4 \Delta\bar{a}(t + \Delta t) \\ \bar{d}^c(t + \Delta t) &= \bar{d}^p(t + \Delta t) - c_5 \Delta\bar{a}(t + \Delta t) \end{aligned} \quad (3-8)$$

where the Gear corrector coefficients are  $c_0 = 3/20$ ,  $c_1 = 251/360$ ,  $c_2 = 1$ ,  $c_3 = 11/18$ ,  $c_4 = 1/6$ , and  $c_5 = 1/60$ , respectively.<sup>48</sup>

### 3.4 Periodic Boundary Condition

In MD simulations, the simulation box size must be large enough to avoid boundary condition artifacts. There are two main kinds of boundary conditions<sup>49</sup>: isolated boundary conditions (IBCs) and periodic boundary conditions (PBCs). In IBCs, the system is surrounded by vacuum, so atoms only interact among themselves. Therefore, IBCs are ideally suited for the study of clusters and molecules. On the other hand, in PBCs, the system is surrounded by infinitely image of the supercell itself in all three dimensions of space, as shown in Fig. 3-2. Hence, an atom may interact not only with atoms in the same supercell but also with atoms in neighboring supercells. In other words, one side of the simulation loops back to the other side, mimicking a bulk phase. In this way, PBCs are suitable for investigating bulk liquids and solids.

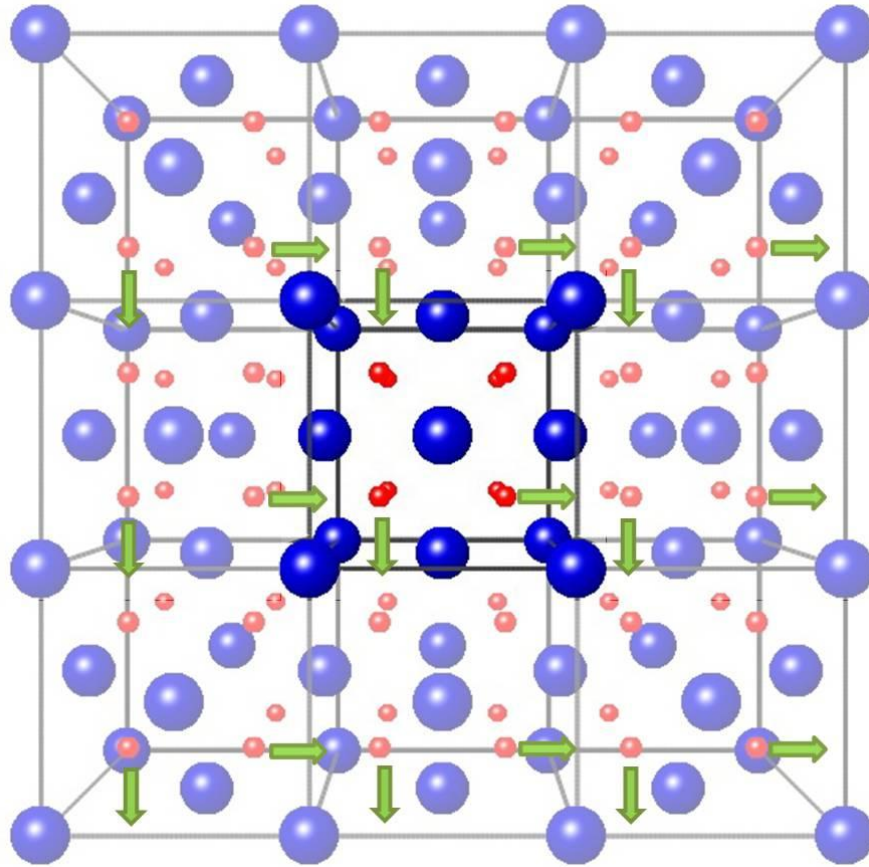


Figure 3-2. Schematic representation of periodic boundary conditions of a fluorite structure supercell. The center box is the actual simulation box.

### 3.5 Interatomic Interactions

For different types of materials, different kinds of interatomic attractions are needed to correctly describe the system. For any given functional form, different parameters can be chosen so as to describe different materials. Therefore, it is essential to define the interatomic interactions before any practical calculations can be performed.

In ionic systems, the potential energy consists of both long-range and short-range interactions. Long range interactions are attractive interactions caused by Coulombic forces. Short-range interactions are mainly repulsive due to overlapping electron orbitals, but there are also some small van der Waals attractive forces. Both types of interactions will be discussed in detail in the following section.

### 3.5.1 Long-Range Interactions

For inorganic materials, especially oxides, long-range forces come from electrostatic interactions, which determine to a large extent the thermodynamic and transport properties. Therefore, precisely evaluating the Coulombic force is essential. In ionic systems, cations and anions are arranged in a defined order. The energy associated with this specific periodicity is the electrostatic attraction energy between two charged ( $q_i$  and  $q_j$ ) ions. The magnitude of the energy ( $E_{long-range}$ ) can be calculated by Coulomb's law:

$$E_{long-range}(r_{ij}) = \frac{q_i q_j}{r_{ij}} \quad (3-9)$$

where  $r_{ij}$  is the distance between ions  $i$  and  $j$ . A negative potential represents an attractive interaction while a positive potential represents a repulsive interaction. Despite the simple formula given above, this is actually the most difficult interaction to evaluate for periodic system.

Since long-range Coulomb's interactions are responsible for the stability of crystalline structures, a critical approximation has to be made to develop an infinite system. It is computationally convenient to have a cutoff truncation beyond a radius or the periodicity of the lattice. Among several methods<sup>50-60</sup>, the Ewald summation<sup>50</sup> and the direct summation<sup>50</sup> are the two most common methods. Though the Ewald summation is more accurate in calculation, it is more computationally intensive than the direct summation. According to the Ewald summation, the high computational load has scaling with system size of  $N^2$ , or better  $N^{3/2}$ , or even at best  $N \log(N)$ .<sup>56-59</sup> In the present study, we are observing the equilibration evolution of point defects, in which the large system requires a larger MD computational cost. As a result, the computationally more efficient

method, direct summation, is applied here. This method has been validated by simulations not only of crystalline but also arbitrarily disordered, charged or neutral ionic systems.<sup>60</sup>

**Direction summation method:** When performing a spherically truncated pairwise  $r^{-1}$  sum in a crystal, the system summed over is never electrically neutral, which essentially leads to non-convergence of the summation. This long-range electrostatic concern can be resolved by an assumption that no basis molecule may be broken up over the entire *Bravais* lattice.<sup>60</sup> For example, rather than regarding the rock salt (or NaCl) lattice as an FCC lattice with a dipolar molecule, one can choose the simple cubic unit with the octopolar (NaCl)<sub>4</sub> basis.<sup>61</sup> This tetra-unit basis is kept together while applying the truncation with the cutoff radius. The direct summation may therefore achieve charge neutrality by introducing additional charge to the truncation sphere. This is not just a mathematical concept; a reconstruction of the polar NiO surface has been observed<sup>62</sup>, and this experimentally upholds the validity of the energy convergence approach.

### 3.5.2 Short-Range Interactions

From Eq. (3-9), the long-range attractive potential between two oppositely charged atoms should bring them closer. In order not to cause structure collapse of the lattice, some repulsive potential must be present to keep the two atoms apart.

The short-range interactions can be expressed by the Buckingham potential:

$$E_{short-range}(r_{ij}) = A_{ij} \cdot \exp\left(-\frac{r_{ij}}{\rho_{ij}}\right) - \frac{C_{ij}}{r_{ij}^6} \quad (3-10)$$

where  $A_{ij}$ ,  $\rho_{ij}$ , and  $C_{ij}$  are empirical parameters;  $r_{ij}$  is the distance between ions  $i$  and  $j$ .

The first term describes the short-range repulsive interactions derived from overlapping electron orbitals, which decrease exponentially with increasing distance between ions  $i$

and  $j$ ; the second term represents the van der Waals attractive contribution due to dipole interactions.

Throughout this study, the short-range interactions are characterized by using the Bushing-Ida<sup>63</sup> type. In addition to the Buckingham potential, a Morse term is included to introduce the “covalent” contribution:

$$E_{short-range}(r_{ij}) = A_{ij} \cdot \exp\left(-\frac{r_{ij}}{\rho_{ij}}\right) - \frac{C_{ij}}{r_{ij}^6} + D_{ij} \left[ \exp(-2\beta_{ij}(r_{ij} - r_{ij}^*)) - 2 \cdot \exp(\beta_{ij}(r_{ij} - r_{ij}^*)) \right] \quad (3-11)$$

where  $D_{ij}$  and  $\beta_{ij}$  are empirical parameters;  $r_{ij}^*$  is the anion-cation  $i$ - $j$  bond length. In a mixed ionic covalent system, the ionic charges are given non-formal values with partial covalence to consider charge transfer between the ions.

Hence, taking into account all interactions acting on an atom associated with surrounding atoms, the energy can be given by:

$$E_{total}(r_{ij}) = \frac{q_i q_j}{r_{ij}} + A_{ij} \cdot \exp\left(-\frac{r_{ij}}{\rho_{ij}}\right) - \frac{C_{ij}}{r_{ij}^6} + D_{ij} \left[ \exp(-2\beta_{ij}(r_{ij} - r_{ij}^*)) - 2 \cdot \exp(\beta_{ij}(r_{ij} - r_{ij}^*)) \right] \quad (3-12)$$

In this thesis, this classical pairwise potential energy form is used. Parameters are taken from Basak *et al.*<sup>64</sup>, as listed in Table 3-1. Fig. 3-3 illustrates the inter-ionic potential energy as a function of distance between  $U^{+2.4}$  and  $O^{-1.2}$  ions.

### 3.5.3 Thermodynamic Conditions (Ensembles) for Simulations

An ensemble is a collection of all possible environmental conditions which have different microscopic states but have an identical macroscopic or thermodynamic state. In MD simulations, certain conditions are assigned in order to obtain desired properties

Table 3-1. Potential parameters used in the present work (Eq. (3-12))<sup>64</sup>

Parameter	Basak <i>et al.</i>
$q_U(e)$	2.40
$q_O(e)$	-1.20
$A_{U-O} (eV)$	693.9297
$\rho_{U-O} (\text{\AA})$	0.3270(22)
$C_{U-O} (eV \text{\AA}^6)$	0.0
$D_{U-O} (eV)$	0.577(45)
$\beta_{U-O} (\text{\AA}^{-1})$	1.65
$r_{U-O}^* (\text{\AA})$	2.369
$A_{O-O} (eV)$	1633.666(6)
$\rho_{O-O} (\text{\AA})$	0.327(022)
$C_{O-O} (eV \text{\AA}^6)$	3.950(63)
$A_{U-U} (eV)$	294.759(3)
$\rho_{U-U} (\text{\AA})$	0.327(022)
$C_{U-U} (eV \text{\AA}^6)$	0.0

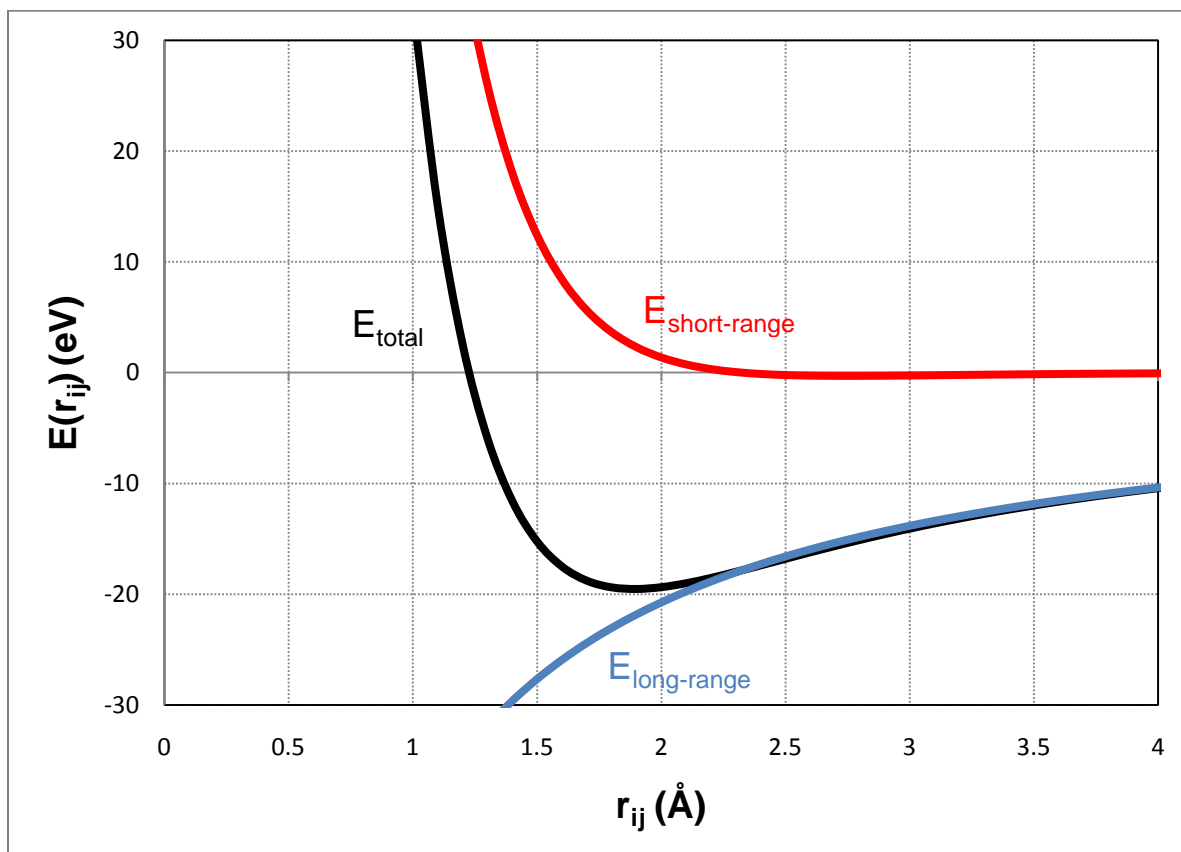


Figure 3-3. Inter-ionic potential as a function of distance between  $U^{+2.4}$  and  $O^{-1.2}$  ions. The total potential ( $E_{total}$ ) is the sum of the long-range Coulombic ( $E_{long-range}$ ) and short-range ( $E_{short-range}$ ) potentials.

of the material, such as total number of atoms, volume, temperature, pressure, etc. A thermodynamic state with fixed number of atoms (  $N$  ), a constant volume (  $V$  ), and a fixed energy (  $E$  ) corresponds to an isolated system, that is, the isochoric micro-canonical ensemble (  $NVE$  ). Similarly,  $NVT$  stands for the canonical ensemble and  $NPT$  refers to the isobaric-isothermal ensemble. These three are the most widely used ensembles, and  $NPT$  is performed throughout this study. In addition, there are also other types of ensembles, such as the grand-canonical ensemble (  $\mu VT$  ) and the isobaric-isoenthalpic ensemble (  $NPH$  ).  $H$  and  $\mu$  represent enthalpy and chemical potential, respectively.<sup>48</sup>

### 3.5.4 Thermostat

In order to control the system simulating at the desired temperature, several approaches have been employed. The simplest one is probably the velocity-rescaling thermostat<sup>48</sup>. Recalling Eq. (3-1), the target velocity (  $V_t$  ) can be rescaled by the following relation:

$$v_t(t) = \sqrt{\frac{T_t}{T_i}} v_i(t) \quad (3-13)$$

where  $T_i$  is the initial temperature;  $V_i$  is the initial velocity;  $T_t$  is the target temperature.

Other popular methods to control the system temperature are Nosé-Hoover<sup>65,66</sup>, Berendsen<sup>67</sup>, and generalized Langevin<sup>68</sup>.

### 3.5.5 Barostat

In addition to the temperature, the volume is another thermodynamic condition needed to be controlled. Various algorithms can be applied to achieve a constant pressure. For example, the idea of the Andersen barostat is to assume that the system is simulated in a container, which is able to be compressed by a piston with certain mass

$m$ .<sup>69</sup> The Lagrangian takes the form:

$$L\left(\rho^N, \dot{\rho}^N, V, \dot{V}\right) = \frac{1}{2} V^{\frac{2}{3}} \sum_{i=1}^N m_i \dot{\rho}_i^2 - \sum_{i<j=1}^N U\left(V^{\frac{1}{3}} \rho_{ij}\right) + \frac{1}{2} m \dot{V}^2 - p_0 V \quad (3-14)$$

where  $\rho$  is the scaled coordinates ( $= r / V^{\frac{1}{3}}$ ;  $r$  is the Cartesian coordinates and  $V$  is the volume);  $p_0$  is the external pressure. The first two terms on the right are just the Lagrangian of the unscaled system. The third term represents a kinetic energy for the piston of mass  $m$  with volume of  $V$ , and the fourth term stands for a potential energy derived from  $p_0$  acting on the piston. However, the Andersen method assumes that the external pressure is hydrostatic, which is not sufficient in all cases. Therefore, Parrinello and Raham further extended this method to anisotropic coupling by allowing the simulation box to change its shape.<sup>70, 71</sup> In this thesis, the P-R method is used.

### 3.6 Conventional Radiation Damage Method by MD Simulations

Atomic-level simulations have long been employed to investigate the fundamental phenomena in radiation damage (RD).<sup>72-76</sup> MD simulations are capable of capturing two major phases: the ballistic phase and the kinetic phase.

Standard MD simulation of radiation damage has been combined with temperature accelerated dynamics (TAD) simulations to achieve the longer and experimental time scale. It has been shown that the defect evolution during the kinetic phase is largely independent of the initial damage created during the ballistic phase.<sup>77,78</sup> Therefore, it can be inferred that it is not necessary to perform the simulation from the beginning because the main job of the ballistic phase is to introduce non-equilibrium point-defects into the system. In other words, starting the simulation directly from the kinetic phase, which is most interesting to us, seems to be more efficient. In addition, since much attention will

be drawn on the kinetic evolution of these point-defects, the recombination and clustering mechanism for each separate kind of point-defect will provide more basic information in the study of RD, which is not accessible for conventional RD MD simulations. As a result, another kinetically-evolving irradiation-induced point-defects method will be introduced in this thesis.

## CHAPTER 4 GRAIN BOUNDARY INFLUENCE ON RADIATION DAMAGE IN UO<sub>2</sub>

### 4.1 Kinetically-Evolving Irradiation-Induced Defects Method by MD Simulation

This kinetically-evolving irradiation-induced defects approach does not replace cascade simulations targeting on elucidating the effect of experimental conditions, such as the dose or the energy of incident species. Instead, this method, which bypasses the ballistic phase, allows a much wider range of different defect conditions to be explored. In this approach, a specific number of Frenkel pairs (FPs) are randomly introduced to the system which is equilibrated at high-temperature (1000 K) for a sufficiently long time. Creating FPs by hand makes it possible to generate defects on a selective sub-lattice or both sub-lattices. To avoid uninteresting but spontaneous recombination events, all vacancies are separated from their counterpart interstitials by a distance greater than the recombination radius. Then the system is equilibrated at 1000 K. The defect structure, unlike rapidly recombining point defects, can have a more significant role in determining the true radiation performances of the material. This study will discuss the following kinetic evolution of the FPs.

### 4.2 Simulation Methodology

#### 4.2.1 MD Simulation

Using the interatomic interaction described in 3.5, the melting point of UO<sub>2</sub> and oxygen sub-lattices were determined to be around  $3450 \pm 50 \text{ K}^{79}$  and  $2200 \text{ K}^{79}$ , which are in fair agreement with the experimental value of  $3100 \text{ K}^{80}$  and  $2600 \text{ K}^{81}$ , respectively. In this work, all simulations have been carried out at 1000 K, which is well below the melting temperature of both the material and sub-lattices. At this temperature, the oxygen interstitials and vacancies have high mobility, whereas the uranium counterparts

have very high migration energy and therefore diffuse less. In addition, this temperature is also in the range of 800-1600 K, typical working temperature in the fuel pellet.

The single-crystal simulation supercell contains  $20 \times 20 \times 20$  cubic fluorite unit cells with 96,000 atoms. The polycrystalline microstructure is a large rectangular box ( $51.7 \times 30.2 \times 5.5$  nm) consisting of 611,010 atoms in six hexagonal equal-sized ( $d = 20$  nm) grains (Fig. 4-1). The crystallographic misorientation between three adjacent grains are 0, 30, and 60 degrees with respect to each other, then the GBs are asymmetric high-angle tilt boundaries. Periodic boundary conditions are applied in all three dimensions. The time step of 0.5 fs is chosen as it gives good energy conservation for several thousand steps in NVE test runs. In order to capture as much of the defect evolution as possible, all simulations have been carried out for more than 1 ns. Two analysis methods to identify point defects will be discussed in the following section.

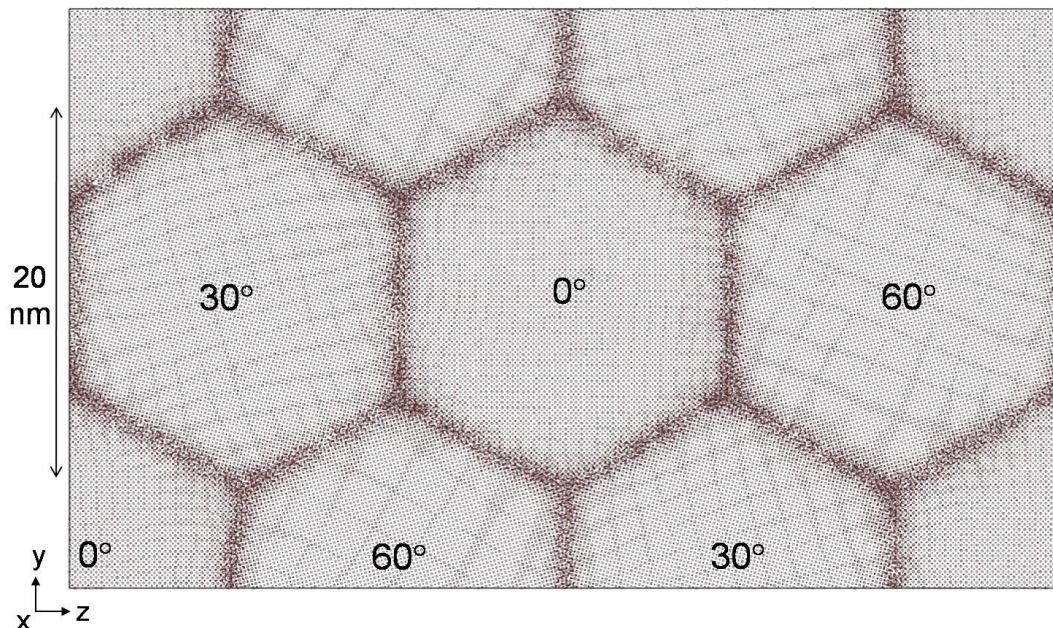


Figure 4-1. Snapshot of the fully equilibrated polycrystalline  $\text{UO}_2$  microstructure with  $d = 20$  nm at 1000 K prior to introduction of defects. The viewing direction is along  $[100]$  columnar axis. Three crystalline orientations are 0, 30, and 60 degrees relative to the columnar axis.

## 4.2.2 Defects Analysis Methods

To observe the kinetic evolution point defects, it is very important to capture the precise number, type, and position of all atoms, especially in the presence of grain boundaries. In fact, the grain boundary is a kind of a defect, so it is relatively valueless to count point defects in the grain boundary.

Here are two methods to perform the analysis. One is the common neighbor analysis; the other is the lattice matching analysis. The two methods are used in complementary manner here.

**Common neighbor analysis (CNA):** As implied in the name, the CNA<sup>82</sup> utilizes the coordination number (CN) of neighboring atoms to identify defects. When it comes to the CN, the cutoff radius plays an important role to determine how far the nearby atom is treated as the neighbor. In  $\text{UO}_2$ , CNs of U atoms are eight and of O atoms are four. As

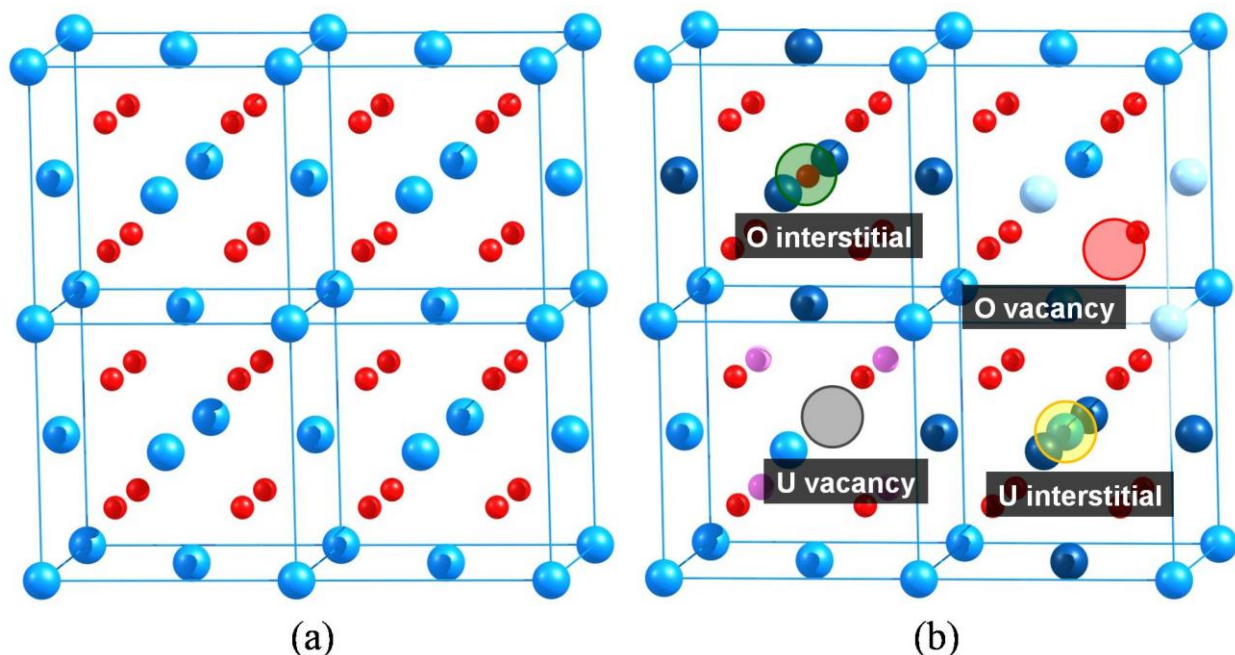


Figure 4-2. Schematic representations of the common neighbor analysis (CNA). (a) Every atom is normally coordinated in the perfect structure (b) There are different coordination numbers (CNs) for the neighboring atoms when defects are present (dark color for higher CNs, light color for lower CNs).

shown in Fig. 4-2 (a), every atom is normally coordinated in the perfect structure. When defects are present (Fig. 4-2 (b)), CNs near interstitials will increase (in darker color) while near vacancies will decrease (in lighter color). In terms of the miscoordination of the defect atom itself and the neighboring atoms, the defect position is identified. However, one big problem is that if there is more than one type of defects close to each other, such as clusters containing both vacancies and interstitials, the CNs will be very complicated to analyze.

**Lattice matching analysis (LMA):** In view of the drawbacks mentioned above, here a second method is also used to identify defects. Considering atoms diffusion at high temperature, the average travelling distance can be calculated. Therefore, a cutoff radius ( $r_{\text{cutoff}}$ ) of  $0.19a_0$  (about  $1.039 \text{ \AA}$ ) is chosen with regard to all lattice sites of the reference structure (Fig. 4-3 (a)), which has been equilibrated for a long time. As a result, if there is

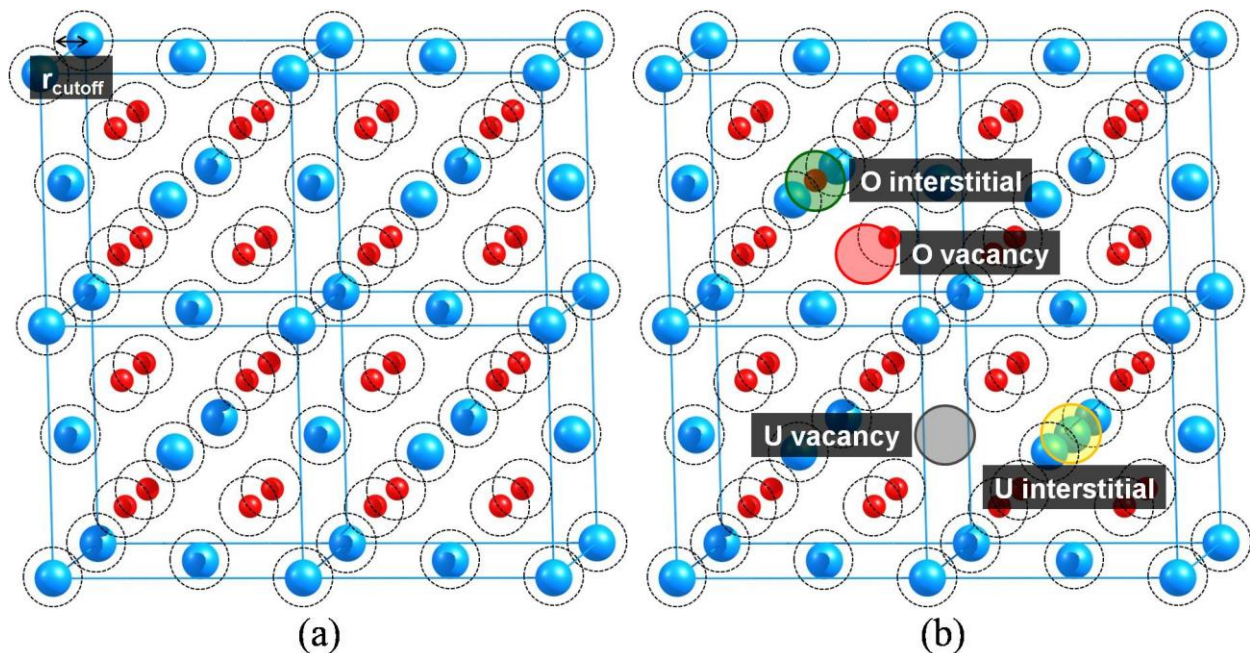


Figure 4-3. Schematic representations of the lattice matching analysis (LMA). (a) A cutoff radius ( $r_{\text{cutoff}}$ ) is assigned to all lattice sites of the reference structure. (b) If there is no atom within the assigned radius, it is a vacancy. If an atom is not within any assigned radius, it is an interstitial.

no atom within the assigned cutoff radius of the original lattice site, the site is regarded as the vacancy. But if there is an atom sitting out of the cutoff circle, the atom will be defined as the interstitial (Fig. 4-3 (b)). Another rare case is that if there is more than one atom within the cutoff circle, all atoms will be reported, such as dumbbell interstitials. With the LMA, we can therefore determine the exact number, type, and position of every point defect.

### 4.3 Results

This work starts with the simpler case, the single crystal, to confirm that simulation methods and tools are correctly implemented. Then the more complicated case, the polycrystal, is investigated.

#### 4.3.1 Frenkel-Pair Defects in Single-Crystal $\text{UO}_2$

The same simulations are run to reproduce previous work by Aidhy *et al.* in single-crystal  $\text{UO}_2$ .<sup>24,37</sup> FPs are created by randomly picking up an ion from its cubic sub-lattice site and placing it at an empty octahedral interstitial site. A defect concentration about 0.21 % was chosen, so 200 was picked up out of 96,000 atoms as defects. Two conditions are performed: (1) 200 FPs only on the U sub-lattice, and (2) 200 FPs on both U and O sub-lattices. Due to the high migration energies of both the U interstitial and vacancy, U FPs have lower diffusivity. On the other hand, both the O interstitial and vacancy have relatively low migration energies, which make them more mobile. Therefore, evolution of the number of U FPs will be less substantial. The results are shown in Fig. 4-4.

**FPs only on the U sub-lattice:** Due to the high migration energy of U interstitials and vacancies, recombination events are less frequent. Out of the initial 200 FPs, 190 U FPs still remain after 1 ns. However, the high concentration of defects on the U sub-lattice

nucleates O FPs. The number of nucleated O FPs is shown by circles in Fig. 4-4. Similar phenomena were also observed by Aidhy *et al.*<sup>24,37</sup> Different from that work, some data within the first 10 ps were analyzed in this work. Interestingly, rather than a gradual increase, the number of O FPs increases abruptly to more than 50, and then decreases to 37 after 10 ps, finally an equilibrium number around 35.

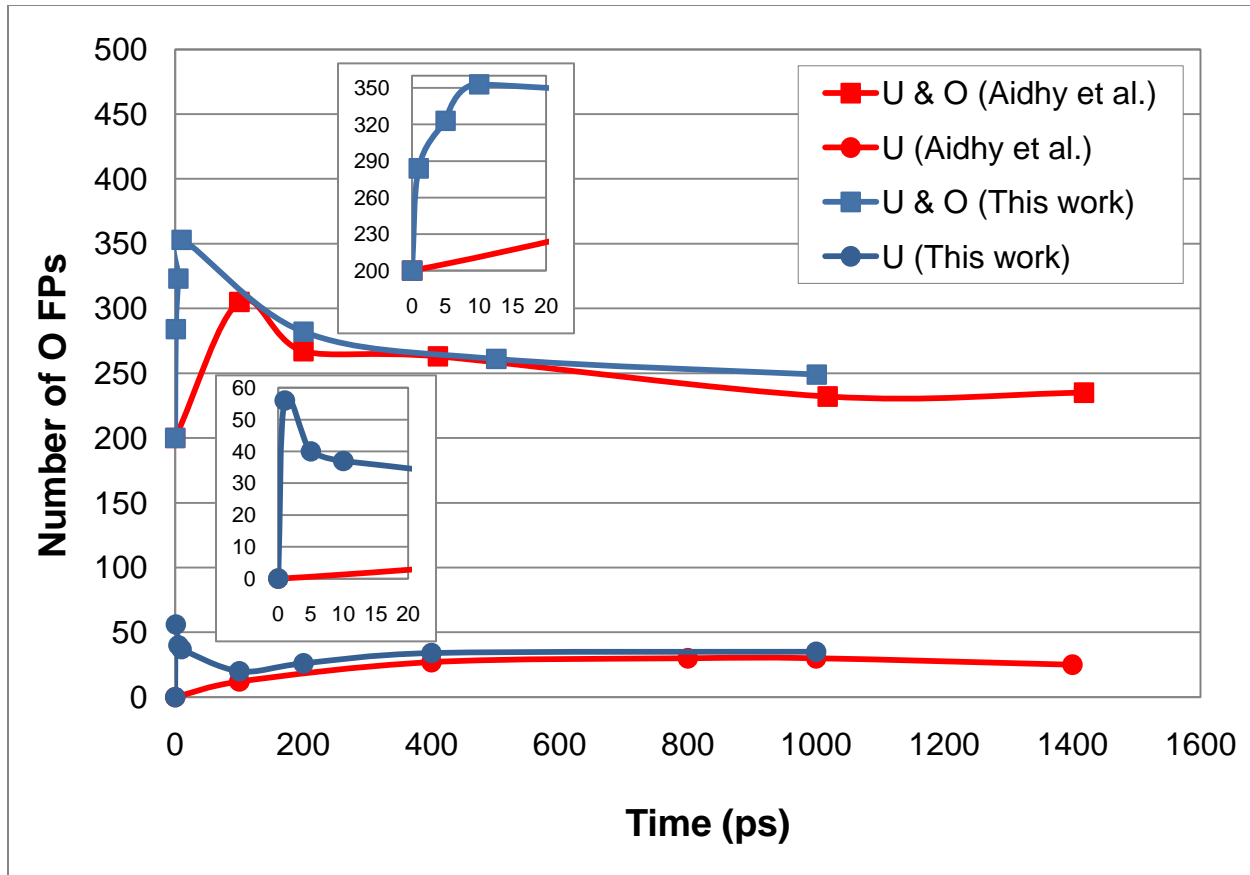


Figure 4-4. Comparison of results from Aidhy *et al.* (red) and this work (blue) for total number of O FPs in two initial conditions: (1) 200 FPs only on the U sub-lattice (circles), and (2) 200 FPs on both U and O sub-lattices (squares). Inset figures are close-up views within the first 10 ps for both conditions.

**FPs on both U and O sub-lattices:** This is a more realistic case in the study of radiation damage. 200 FPs are simultaneously created on both U and O sub-lattices. Based on simulations on the U sub-lattice alone, most of U FPs remain at their initial sites because of their low diffusivities. In contrast, a considerable increase in the number of O FPs

takes place within the first 200 ps, as shown by the squares in Fig. 4-4. Afterwards, the number is followed by a decline to the equilibrium number to around 250. Instead of complete annihilation of O FPs, the number is actually larger than that of the initial concentration (200 FPs).

From the above simulation run, it can be indicated that these signatures are consistent with the previous results from Aidhy *et al.* In addition, more information taking place within the first few picoseconds shows that the high concentration of defects on the U sub-lattice nucleates O FPs in a very fast manner.

#### **4.3.2 Frenkel-Pair Defects in Polycrystalline UO<sub>2</sub>**

For a more representative of the real material, polycrystalline UO<sub>2</sub> is investigated. Before generating the defects, the polycrystalline structure is first equilibrated at the working temperature (1000 K) for 1 ns to ensure no spontaneous formation of defects. Given that the formation energies for O FPs and U FPs are 6.0 and 17.0 eV<sup>83</sup> with the Basak potential<sup>64</sup>, the defect concentration of  $5.8 \times 10^{-31}$  and  $2.1 \times 10^{-86}$  would be expected in this simulation. Consistent with this, no defects are present in the bulk grain region. This equilibrated structure is used as the initial structure for rest of the simulations and as the reference structure in the LMA. In order to perform a simulation under similar conditions to the previous single-crystal work, 185 FPs are introduced to selected grains of the polycrystal. The defect concentration relative to the bulk (eliminating atoms in GBs) corresponds to 200 FPs in the single crystal containing 96,000 atoms. Three different scenarios are analyzed for each of the single grains: (1) 185 FPs only on the U sub-lattice, (2) 185 FPs only on the O sub-lattice, and (3) 185 FPs on both U and O sub-lattices. All FPs are introduced to the bulk region. All types of vacancies are

separated from their counterpart interstitials by  $1.5a_0$ . The structure is then equilibrated at 1000 K with the NPT ensemble for 1 ns.

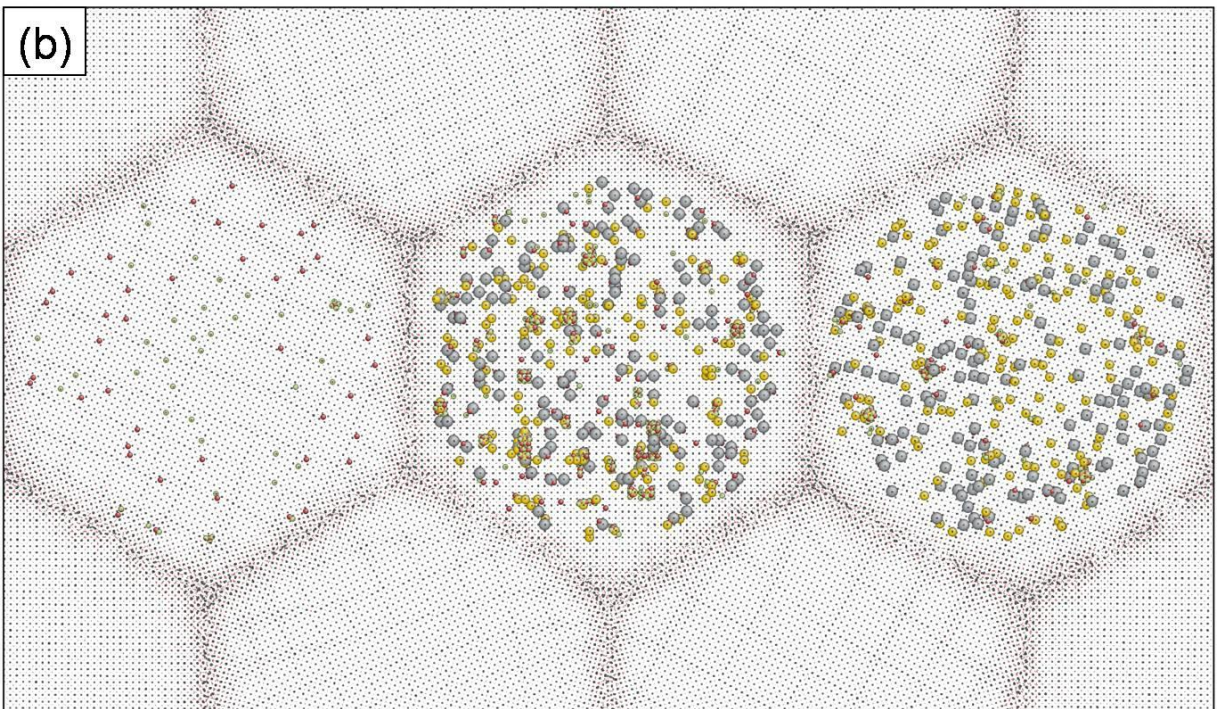
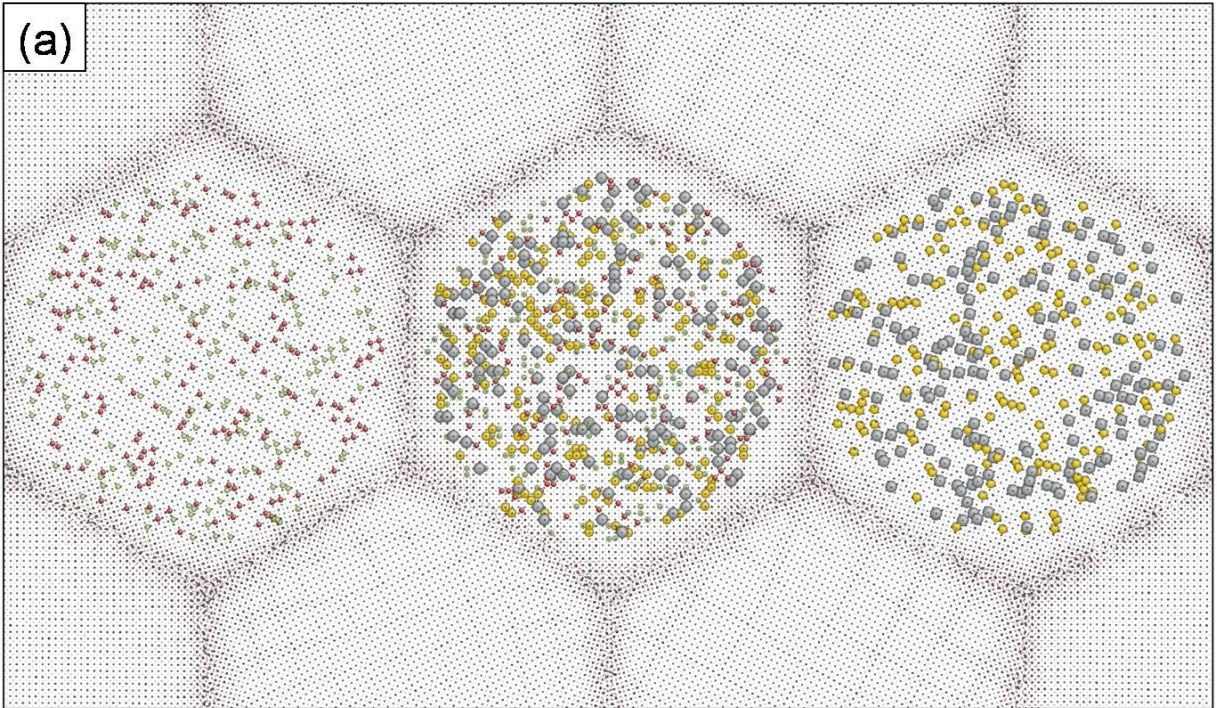
**FPs only on the O sub-lattice:** A snapshot of the initial structure is shown in Fig. 4-5 (a) (left grain, Grain 1). Due to the low migration energies of both O interstitials and vacancies, O FPs are more mobile, which means they have higher diffusivities. The number of O defects is shown in Fig. 4.6 (green triangles). After the first 25 ps, only 44 out of 185 O FPs are left (Fig. 4-6 (b)). Most of the O FPs are annihilated by vacancy-interstitial recombination mechanism. After 400 ps, fewer than 10 O FPs are sporadically present (Fig. 4-6 (d)). Nevertheless, after 100 ps the number of O vacancies is 3 greater than the number of O interstitials because a V-4O vacancy-interstitial clusters forms. This kind of cluster will be discussed in detail later. However, no interstitial-interstitial or vacancy-vacancy cluster is observed, which indicates that in the absence of defects on U (or cation) sub-lattice, the defects on O sub-lattice (or anion) are almost healed within a few picoseconds. As a result, there will be no long-lasting damage to the material.

**FPs only on the U sub-lattice:** The initial snapshot is shown in Fig. 4-5 (a) (right grain, Grain 3). Within first 400 ps, only 27 U FPs out of 185 U FPs have been recovered. Similar to the case in single crystal, the high migration energy of U interstitials and vacancies makes U FPs unable to recombine. Therefore, the remaining high concentration of defects on the U sub-lattice nucleates new O FPs. The nucleation processes seem to occur rapidly right at the onset of the equilibration. As shown in Fig. 4-6 (red circles), the number of O interstitials and vacancies increases with a very steep slope in the beginning. Different from the case in the single crystal, it is followed by an

equilibrium plateau rather than a slow decrease. What should be noted here is that the equilibrium number of O defects is much larger (about three to four times) than that in single crystal. The equilibrium number of O defects is determined by competition between two phenomena taking place simultaneously: (1) random diffusion of O FPs leading to annihilation by recombination, and (2) GBs being the source and sink of O FPs. In the single crystal, there are no GBs, so the number of O FPs solely depends on the recombination rate. Nevertheless, with the presence of GBs in polycrystal, the source/sink behavior will influence the defect concentration. In addition, there are some clusters being observed, such as V-4O clusters, Schottky defects, and cuboctahedral (COT) clusters. This will also be discussed in detail later.

**FPs on both U and O sub-lattices:** Fig. 4-5 (a) (center grain, Grain 2) shows the snapshot of the initial structure with 185 FPs on both U and O sub-lattices simultaneously. As observing in the previous simulation of defects on the U sub-lattice alone, there is no distinct change in the number of U FPs, but there is a substantial increase of O FPs, as shown in Fig. 4-6 (blue squares). However, it has to be noted that the number of O interstitials is always smaller than that of O vacancies by about 30 after first 100 ps. A similar phenomenon is also observed in the case of FPs on the U sub-lattice alone. This is because GBs can behave as a source or sink for vacancies but only as a sink for interstitials, which will be discussed in detail in the next section. In both these two conditions, the total number of clusters is larger due to higher initial defect concentration on the U-sub-lattice.

In the single crystal, the number of vacancies and interstitials has to be equal in order to achieve electroneutrality. In the polycrystal, the overall system still requires



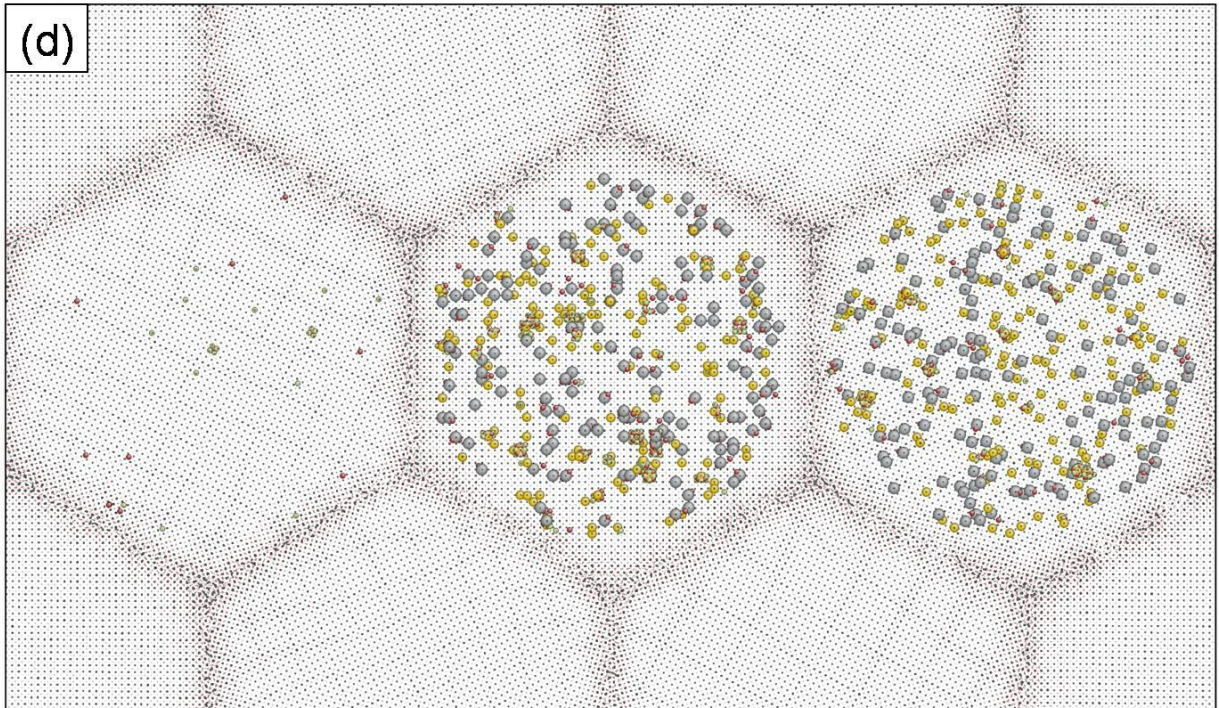
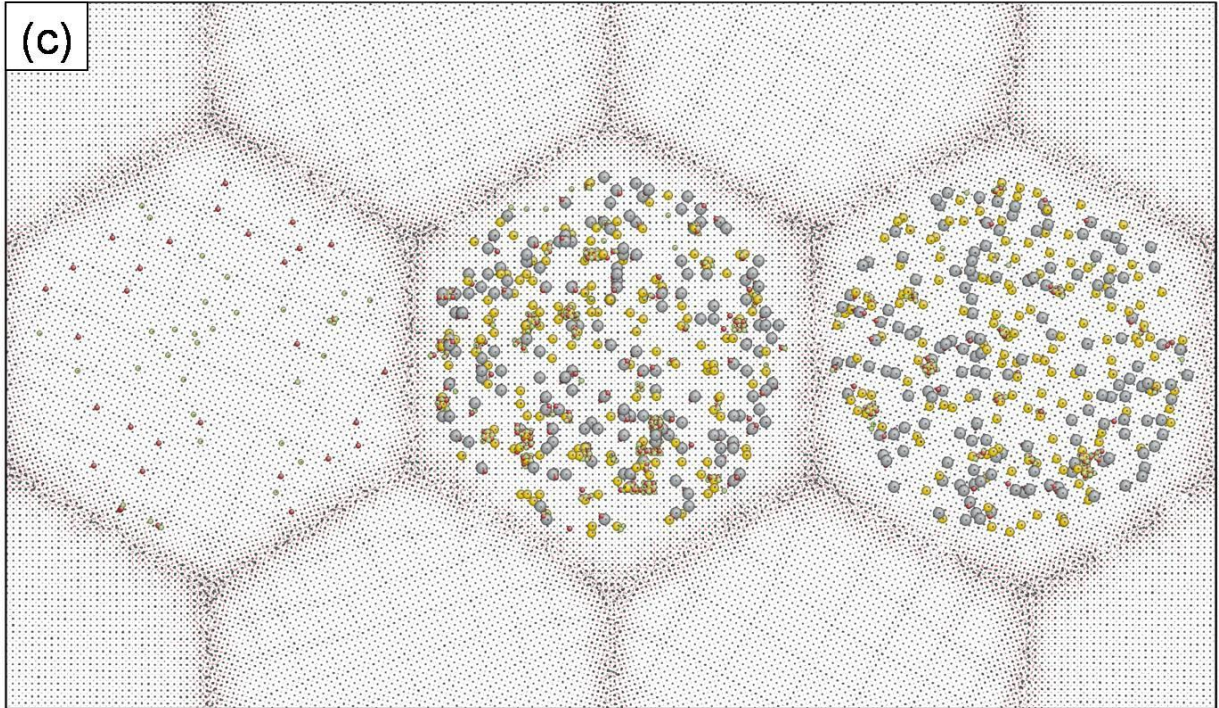


Figure 4-5. Evolution of point defect (small circles in green and red for oxygen interstitials and vacancies, large circles in yellow and grey for uranium interstitials and vacancies). Snapshots taken at (a) 0 ps, (b) 25 ps, (c) 50 ps, and (d) 400 ps. All defects are in superposed on the initial structure without introduction of any defects.

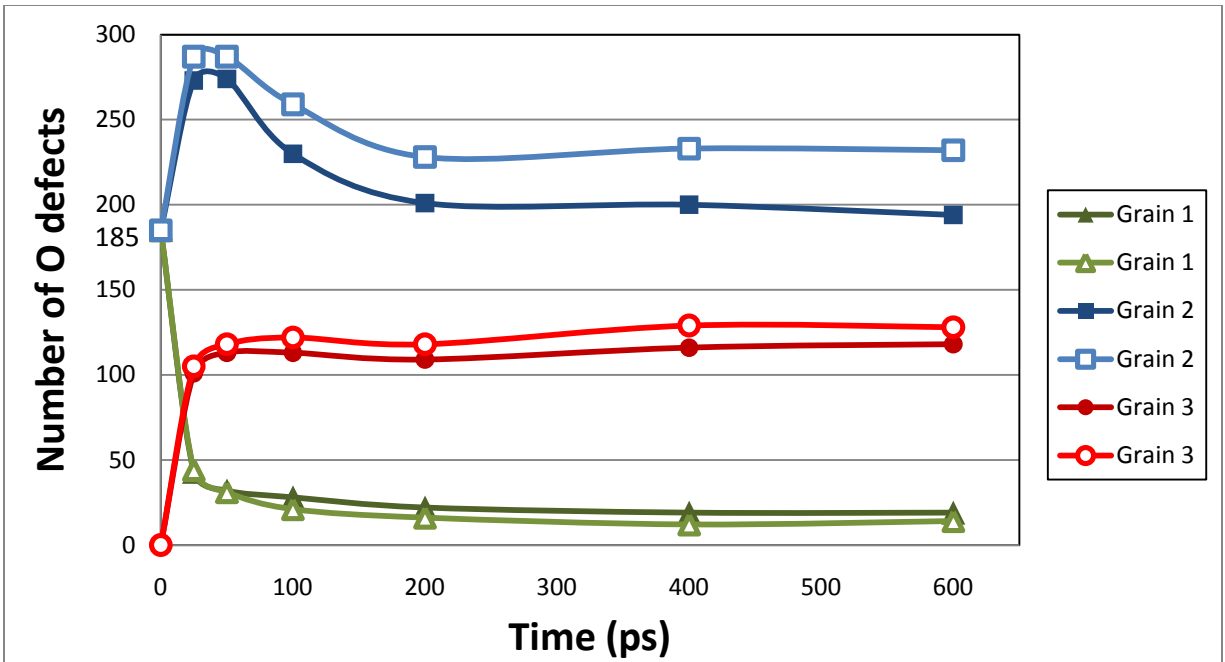


Figure 4-6. Number of O defect showing up in the bulk grain in three initial conditions: (1) 185 FPs only on the U sub-lattice (circle), (2) 185 FPs only on the O sub-lattice (triangle), and (3) 185 FPs on both U and O sub-lattices (square). Solid and open notations stand for interstitials and vacancies, respectively.

charge neutrality; however, the results show that there are some differences between the number of vacancies and interstitials. It can be assumed that when some of the defects form clusters, the bulk region may not be electroneutral. Therefore, GBs will play the role of maintaining the charge neutrality in the bulk by modulating the defect concentration via source/sink behaviors of point defects. Hence, we will take a closer look to see how GBs interact with these defects.

#### 4.3.3 Grain Boundary Source/Sink Behaviors for Point Defects

The major difference in the defect evolution between the single crystal and the polycrystal is the presence of GBs. Here specific interaction mechanisms between GBs and point defects will be characterized. Since uranium vacancies and interstitials have low migration energies and are less mobile, attention will be focused only on the more interesting oxygen vacancies and interstitials.

**GBs as vacancy sources:** The emission of a vacancy from the GB is presumably a thermally-activated process that is associated with an attempt frequency.<sup>84</sup> GBs may produce many vacancies and reabsorb them before a successful emission occurs in which the vacancy can sufficiently distance itself into the grain.<sup>85</sup> An example is demonstrated in Fig. 4-7; the red circle indicates the location of the oxygen vacancy because an oxygen atom is missing from the column which should have specific number of oxygen atoms. In Fig. 4-7 (a), a snapshot taken at 20.5 ps, the circled vacancy is one of many vacancies produced by the GB, and now it is ready to go into the interior grain. As time progresses, the vacancy diffuses further from the GB (Fig. 4-7 (b)-(e)). Fig.4-8 gives close-up views of each snapshot in Fig. 4-7, illustrating the mechanism for the vacancy moving into the grain. The viewing direction is also along [100]; larger spheres are uranium atoms; smaller spheres are oxygen atoms; the purple area (defined by the presence of many miscoordinated atoms) refers to the GB region shown in Fig.4-7; the big red circle sitting on the oxygen column describes a missing oxygen atom in that column, i.e. the approximate vacancy position; small black circles represent positions of specific oxygen atoms involved in this diffusion activity (here, the small black circle 1 in the figure will be notated as O-1 in the following text for convenience). From Fig. 4-8 (a) to (b), O-1 goes into the GB to the original site of the vacancy, followed by O-2 filling in the vacant site of O-1. Therefore, a macroscopic view showing that the vacancy emits from the GB to where O-2 was. This diffusion mechanism is referred to the interstitialcy mechanism, in which the moving direction of the defect and the atom are opposite. Similar diffusion mechanism takes place from (c) to (e), so the vacancy finally resides in the original site of O-7.

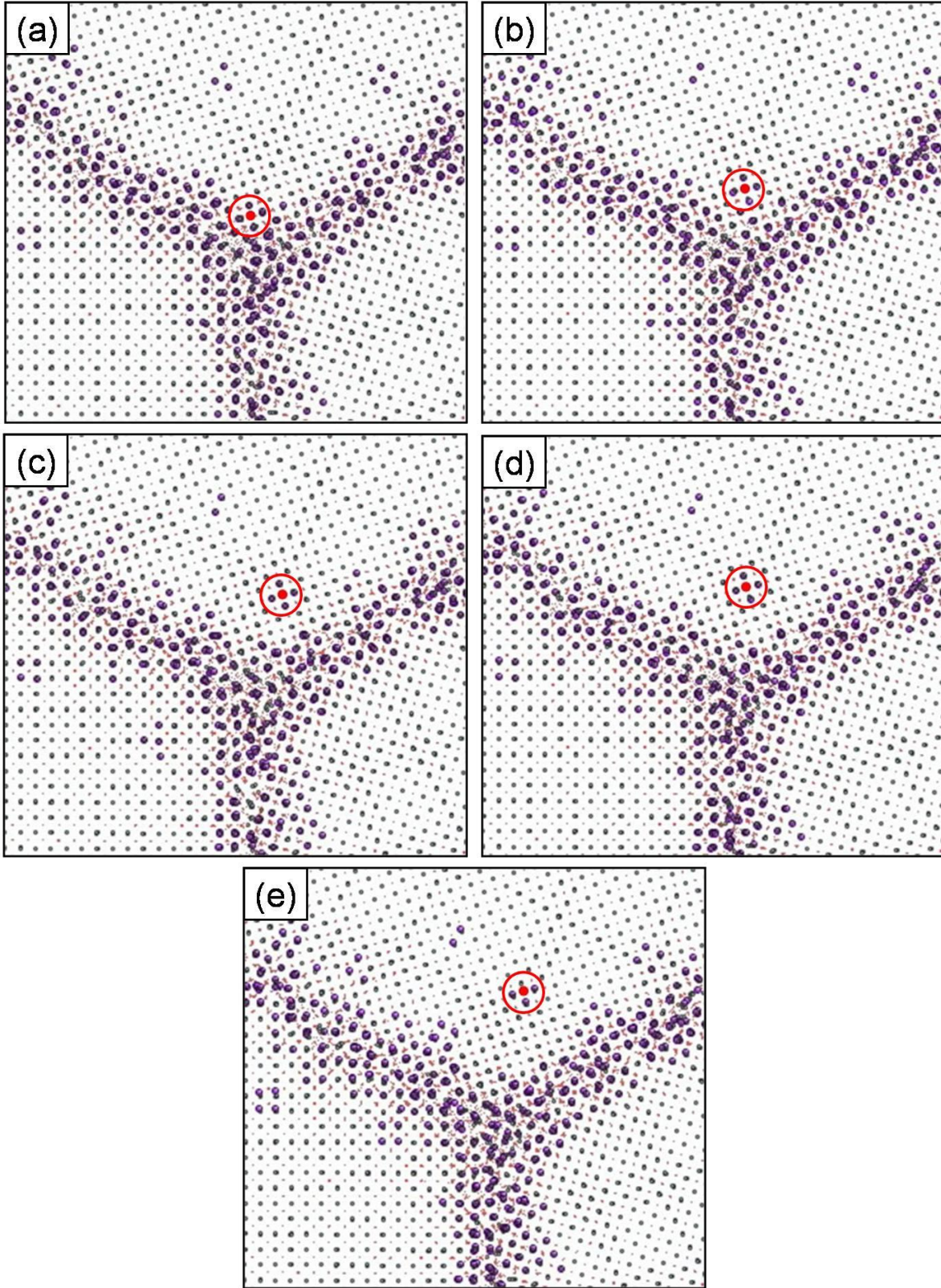


Figure 4-7. Progressive snapshots showing the GB being the source for the O vacancy (red) taken at (a) 20.5 ps, (b) 21 ps, (c) 21.5 ps, (d) 23.5 ps, and (e) 24.5 ps.

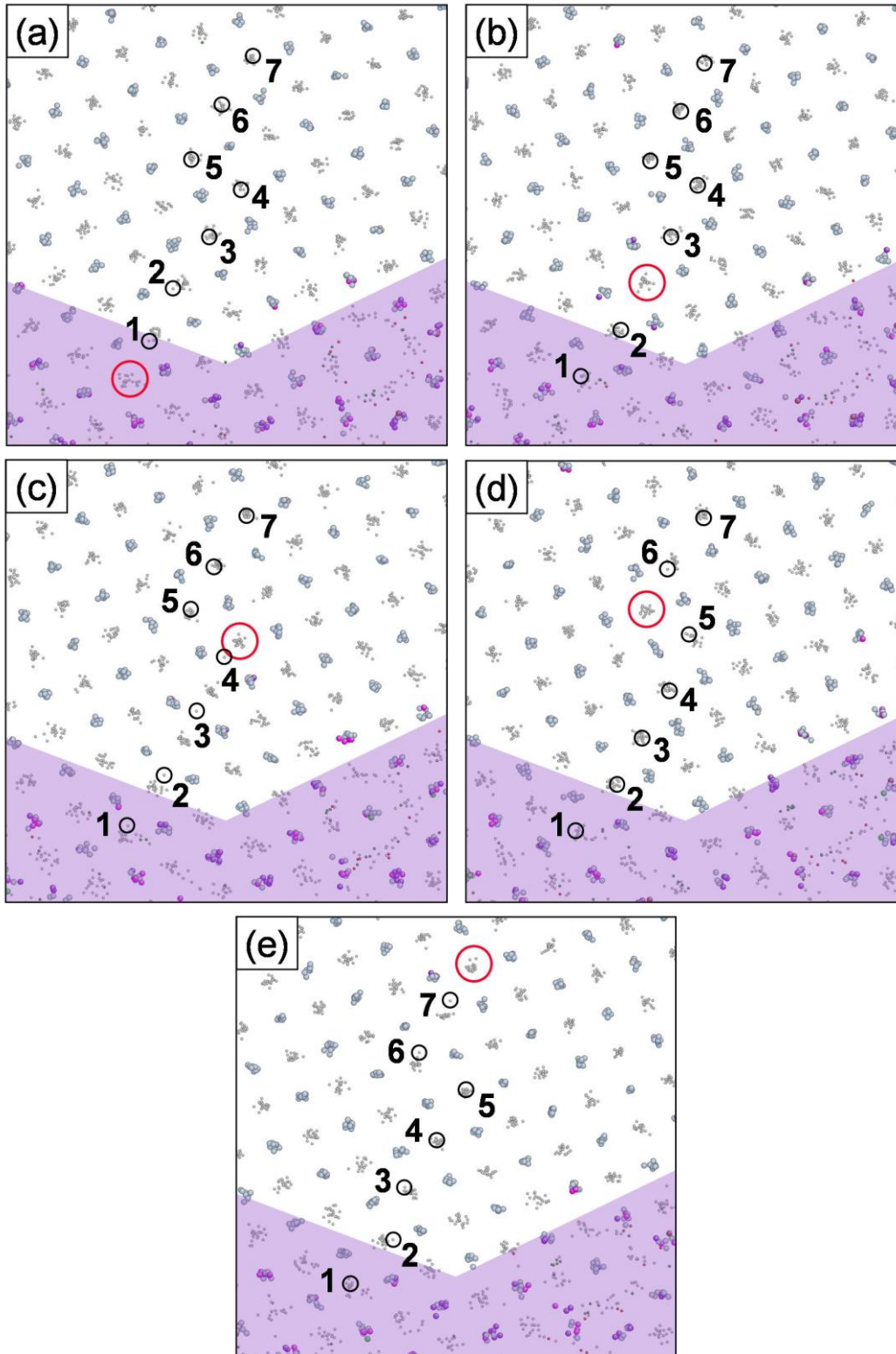


Figure 4-8. Close-up views of the GB being the source for the O vacancy taken at (a) 20.5 ps, (b) 21 ps, (c) 21.5 ps, (d) 23.5 ps, and (e) 24.5 ps. The purple area refers to the GB region; the labeled oxygen atoms are involved in this activity; the large red circle indicates the location of the vacancy.

**GBs as vacancy sinks:** GBs, in addition to being vacancy sources, can also operate as sinks for both vacancies and interstitials. Fig. 4-9 demonstrates an example of the GB being the vacancy sink. The snapshot taken at 9 ps shows that the vacancy is still in the grain but near the GB (Fig. 4-9 (a)). After 0.5 ps, the vacancy is closer to the GB (Fig. 4-9(b)) and finally absorbed by the GB at 10 ps (Fig. 4-9(c)). This vacancy does not re-emerge after 12.5 ps. The interstitialcy diffusion mechanism is illustrated in close-up views of Fig. 4-10 with respect to Fig. 4-9. The original vacancy site is filled by O-1, followed by O-2 taking the place of the vacant site of O-1, so the vacancy is macroscopically absorbed by the GB. However, it turns out that O-2 is initially not quite in

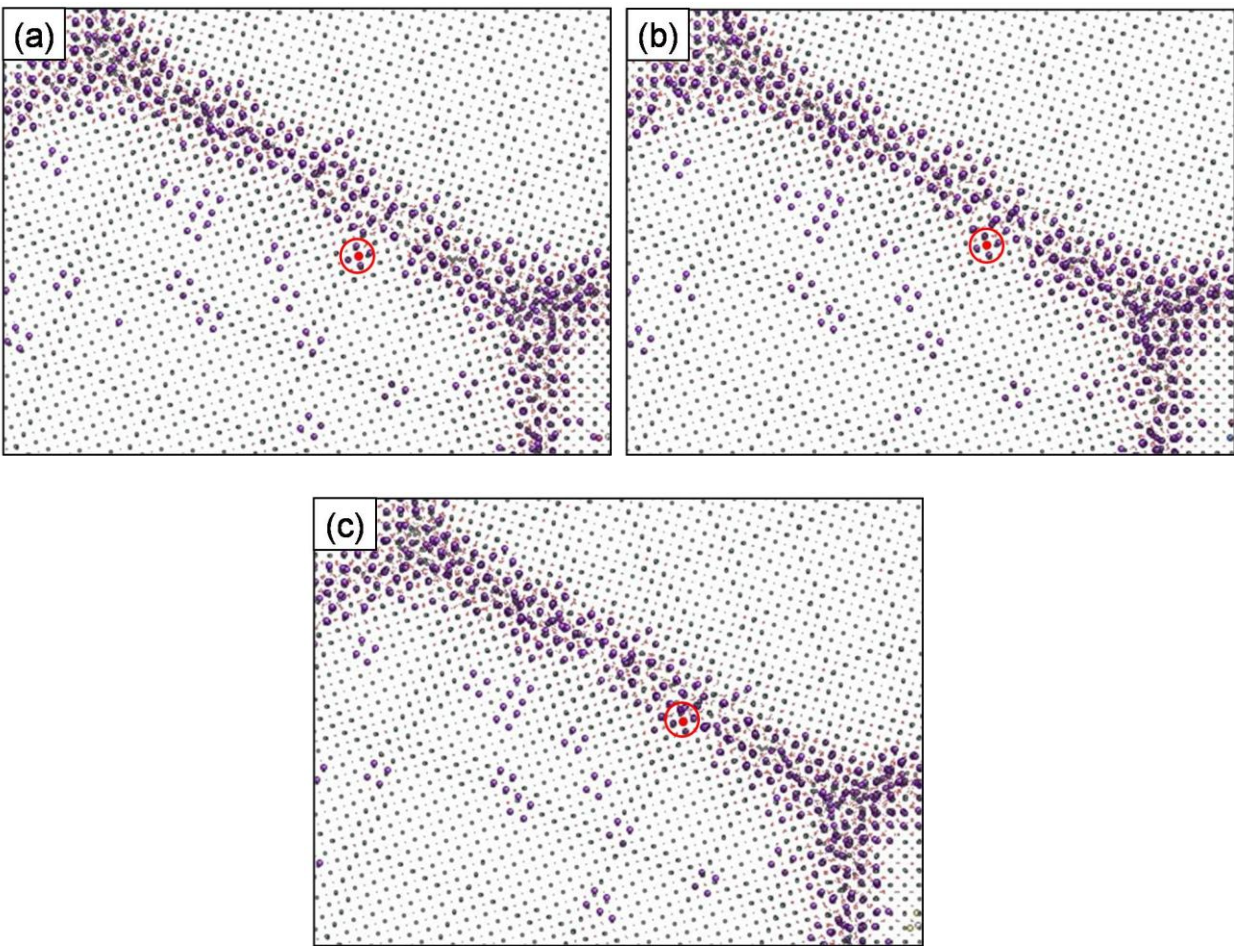


Figure 4-9. Progressive snapshots showing the GB being the sink for the O vacancy (red) taken at (a) 9 ps, (b) 9.5 ps, (c) and 10 ps.

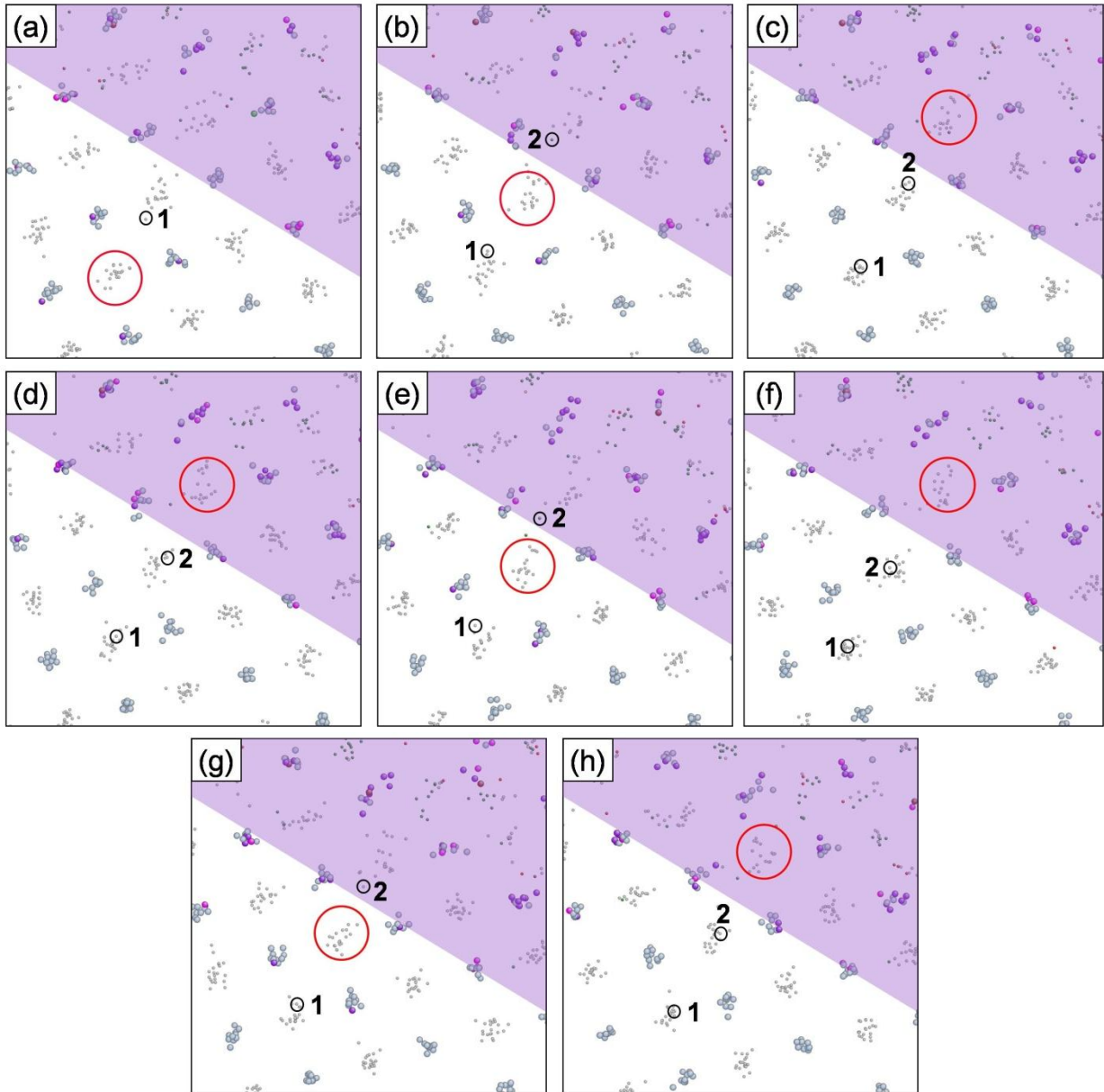


Figure 4-10. Close-up views of the GB being the sink for the O vacancy taken at (a) 9 ps, (b) 9.5 ps, (c) 10 ps, (d) 10.5 ps, (e) 11 ps, (f) 11.5 ps, (g) 12 ps, and (h) 12.5 ps. The purple area refers to the GB region; the labeled oxygen atoms are involved in this activity; the large green circle indicates the location of the vacancy.

equilibrium in that vacant site. Fig. 4-10 (d) to (h) exhibits O-2 moving back and forth between the GB and the grain, but finally sitting in the site that O-1 originally was. This indicates that the thermally-activated diffusion process is not a one-time and one-step

process. Instead, the process requires some attempts to find the most favorable site before the “successful” interstitialcy diffusion.

It also has to be noted that atoms look to be better aligned in the columnar fashion at position O-2 in the Fig. 4-10 (c) than the same column in (b). Therefore, Fig. 4-11 shows single point alignment offsets at positions O-1 (blue triangles) and O-2 (red squares) in Fig. 4-10 (c) calculated from 9 ps to 12.5 ps, referring to Fig. 4-10 (a) to (h). The offset is with respect to the oxygen columnar axis viewing along [100] direction. From Fig. 4-11, the highest offset of position O-1 is at 9.5 ps, when O-1 is participating in the vacancy diffusion; the highest offset of position O-2 is at 11 ps, when O-2 is also taking part in the vacancy diffusion. In addition, the offset of position O-2 is always larger than that of position O-1 because position O-2 is closer to the GB area, which is characteristically disorder. Offsets for both positions finally decrease after the vacancy is “successfully” absorbed by the GB, which also indicates that the damage is healed in a more macroscopic sense.

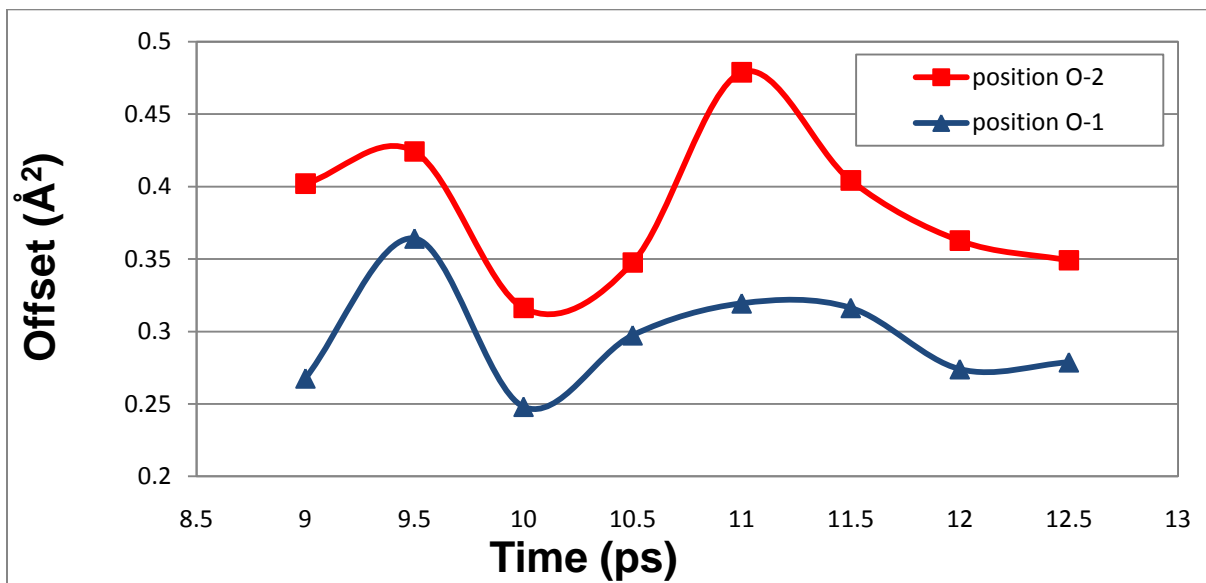


Figure 4-11. Single point alignment offsets at positions O-1 and O-2 in Fig. 4-10 (c) with respect to the time from Fig. 4-10 (a) to (h).

So far, evidence has been shown that GBs can nucleate and annihilate vacancies. As for interstitials, there are some differences from vacancies.

**GBs as interstitial sinks:** Annihilation of interstitials by the GB is also observed, as shown in Fig.4-12. In a similar manner, the snapshot taken at 6.5 ps displays that the circled interstitial (green) is far from the GB and is not ready to diffuse (Fig. 4-12 (a)). At 10 ps, the interstitial is still in the same site, but atoms between it and the GB are no longer in a columnar alignment (Fig. 4-12 (b)). This disorder is thermally activated by some atoms acquiring enough energy to make jumps, and this actually paves the way for the interstitial to move towards the GB, finally disappearing in the GB, as shown in Fig. 4-12 (c) to (e). These phenomena can be further focused in close-up views in Fig. 4-13. Especially in (c), a maximum randomness appears for the column occupied by O-3, O-4, O-5, O-6, and O-7. It turns out that only three of them can stay, so O-6 moves into the GB and O-7 goes back to its original site, leaving O-3, O-4, and O-5 behind. Similarly, the rearrangement of atoms makes them more aligned in Fig. 4-13 (e) than in (c).

From the study of defects evolution above, interstitials diffusing into the GB, vacancies coming out of the GB and diffusing back to the GB are observed. It should be noted that no interstitials are observed to come out of the GB. Therefore, it can be inferred that GBs can be sources or sinks for vacancies but only sinks for interstitials. It has been reported by a radiation damage simulation research in copper that the formation energy of interstitials at the GB is smaller than in the bulk. Therefore, the formation energy of oxygen interstitials at the GB can also be smaller than in the bulk. With this assumption, there is a barrier for interstitials to re-enter the perfect bulk. As a result, no interstitials will be emitted from GBs.

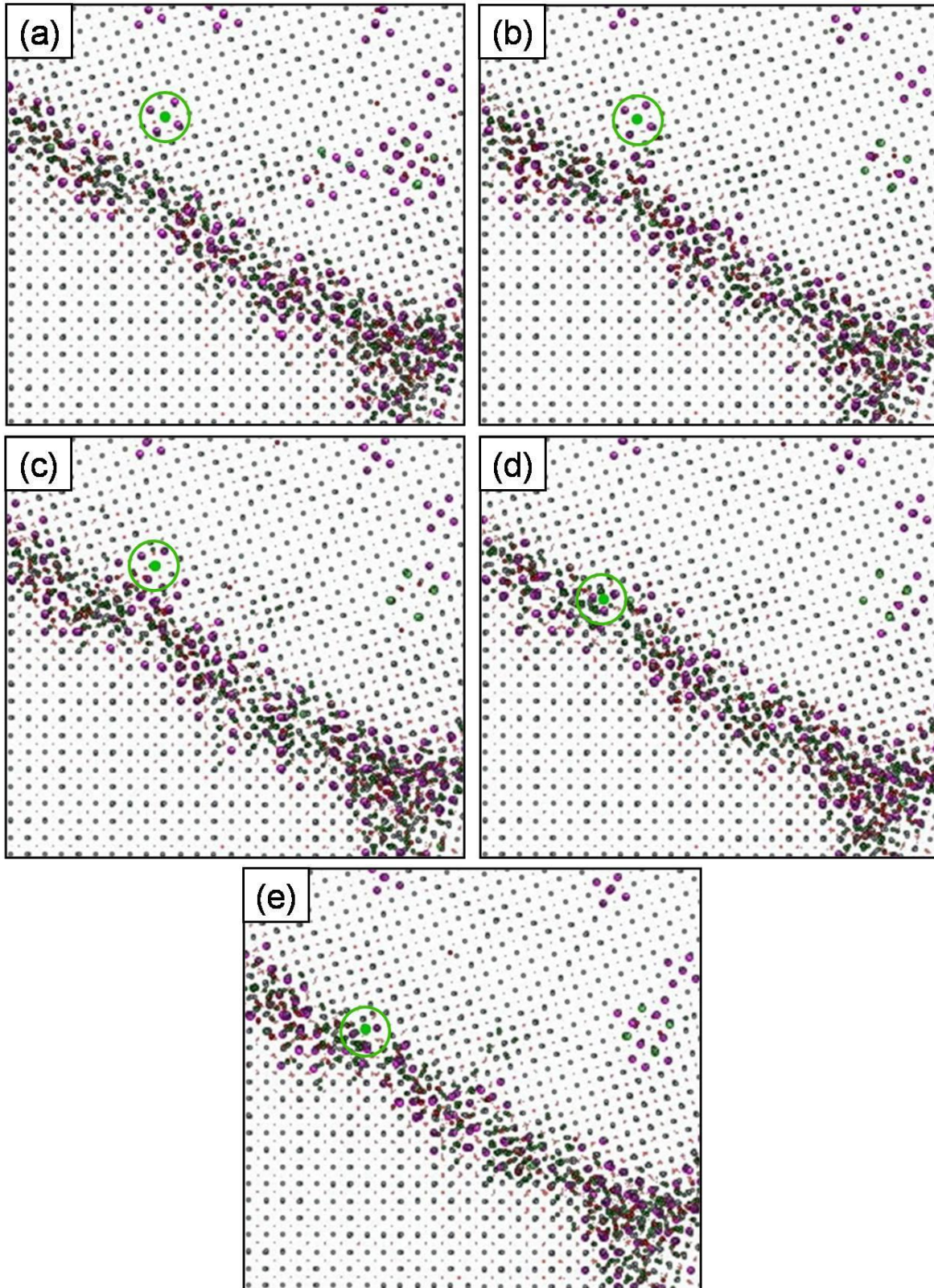


Figure 4-12. Progressive snapshots showing the GB being the sink for the O interstitial (green) taken at (a) 6.5 ps, (b) 10 ps, (c) 10.5 ps, (d) 11 ps, and (e) 15 ps.

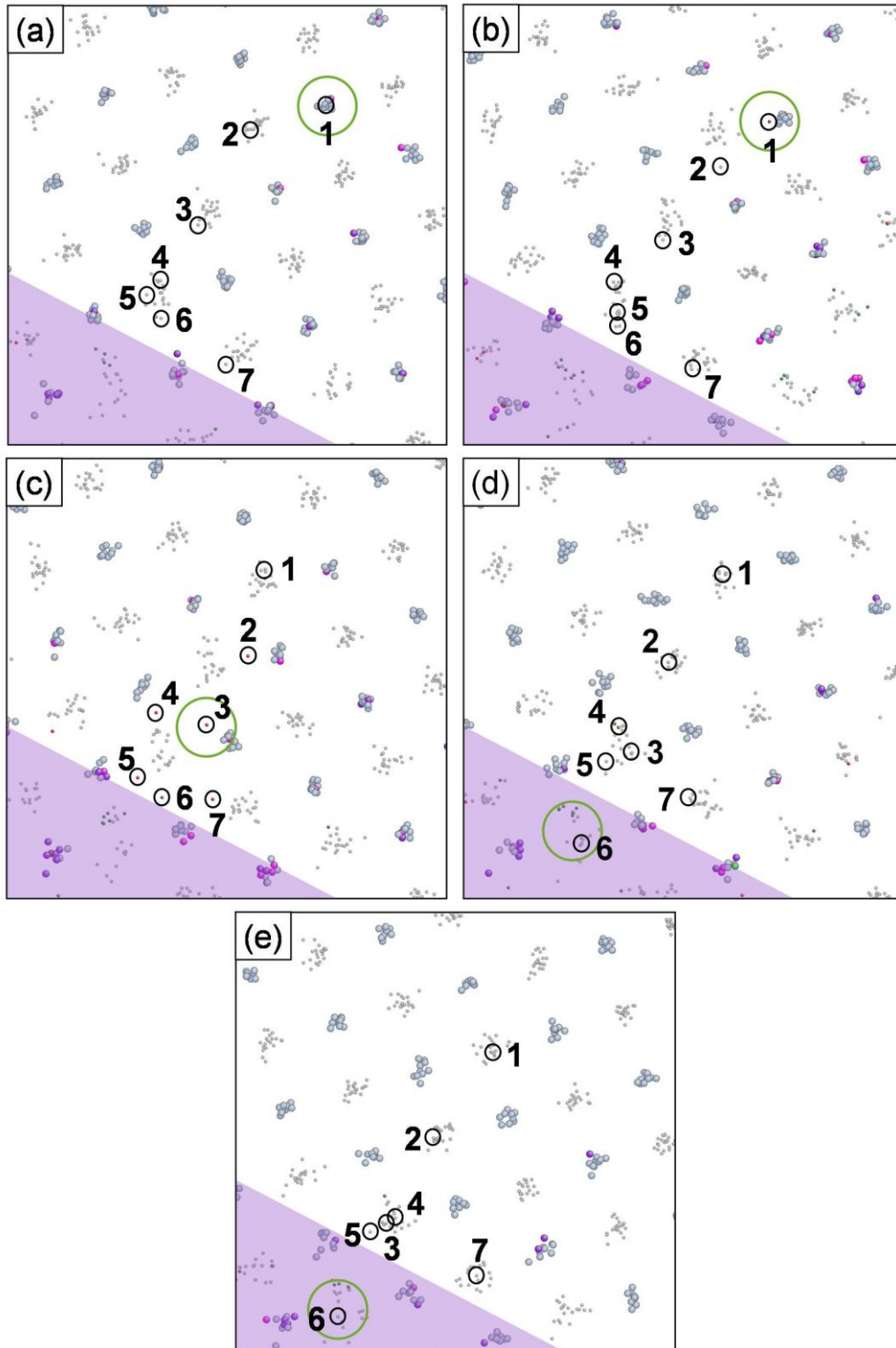


Figure 4-13. Close-up views of the GB being the sink for the O interstitial taken at (a) 6.5 ps, (b) 10 ps, (c) 10.5 ps, (d) 11 ps, and (e) 15 ps. The purple area refers to the GB region; the labeled oxygen atoms are involved in this activity; the large green circle indicates the location of the interstitial.

The diffusion mechanism was qualitatively described above, and now some quantitative analyses will be performed in order to fully characterize the diffusion.

To take a specific example, in the second case of GBs being the vacancy sink, it can be seen from Fig. 4-9 (b) to (c) that the vacancy travel about 1.6 Å along [010] direction within 0.5 ps. This diffusion distance is less than the first nearest neighbor distance (2.7 Å) in the single crystal.

To ascertain if this rate of vacancy diffusion is reasonable or not, recall Eq. 2-6 that the diffusivity has a temperature-dependence:

$$D = D_0 \cdot \exp\left(-\frac{\Delta H_m^*}{RT}\right) \quad (2-6)$$

using the diffusion parameters from Govers *et al.*<sup>86</sup> for  $\text{UO}_{2-x}$  with the Basak potential. The pre-exponential diffusivity ( $D_0$ ) is 0.00045 cm<sup>2</sup>/s and the migration enthalpy barrier ( $\Delta H_m^*$ ) is 0.45 eV. With the equilibration under 1000 K, the atom diffusivity ( $D_A$ ) can be estimated to be about  $2.4 \times 10^{-2}$  Å<sup>2</sup>/ps.

The atom diffusivity is therefore calculated from the Eq. 2-14 with the correlation factor  $f_v = 0.653$  for the free vacancy,  $c_v = 1.5 \times 10^{-3}$ , and  $c_A \approx 1$ .

$$D_A c_A = f_v D_v c_v = f_i D_i c_i \quad (2-14)$$

The calculation gives the atom diffusivity ( $D_V$ ) to be about 24.8 Å<sup>2</sup>/ps.

In simulations, the self-diffusion distance of the vacancy can be evaluated by Eq. 2-22:

$$D_V = \frac{1}{6t} \langle |\bar{r}_i - \bar{r}_0|^2 \rangle \quad (2-22)$$

So the diffusion distance is determined to be about 8.6 Å. Compared with 1.6 Å from the observation, it is of the same order of magnitude. In addition, the diffusion direction is

also consistent with the primary oxygen diffusion pathway,  $\langle 001 \rangle$  direction, for the fluorite-based material.<sup>87</sup> The discrepancy of the value may come from evaluation by an only single diffusion event in a very short observation time. In order to obtain high accuracy, the diffusion rate should be estimated by an average of multiple diffusion events for a longer time period.

#### 4.3.4 Vacancy Clustering: Schottky Defects

A Schottky defect is composed of one U vacancy and two O vacancies. The formation of Schottky defects are observed in the presence of U FPs, that is, the condition of defects on the U sub-lattice alone and on both U and O sub-lattices.

Evidence has been shown that the  $V_{\text{O}}^{\bullet\bullet} - V_{\text{U}}^{\bullet\bullet\bullet} - V_{\text{O}}^{\bullet\bullet}$  Schottky (neutral tri-vacancies)

defect cluster is more stable than either the  $V_{\text{O}}^{\bullet\bullet} - V_{\text{U}}^{\bullet\bullet\bullet}$  di-cluster or entirely separated

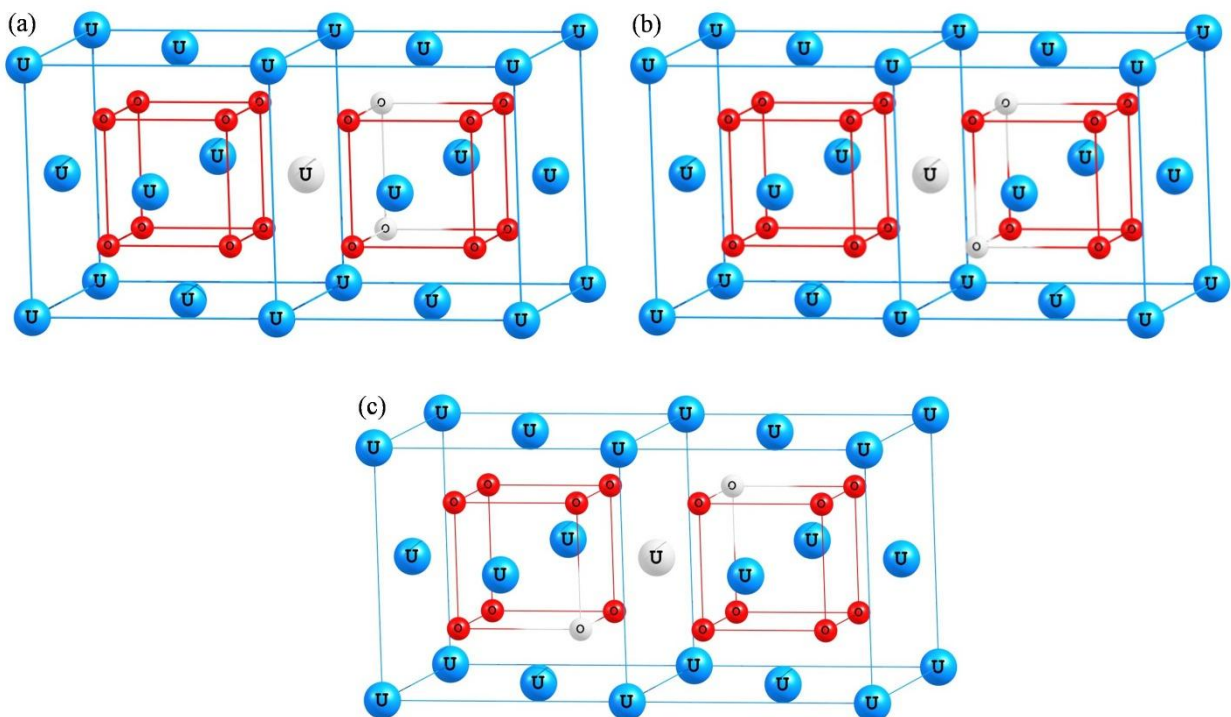


Figure 4-14. Schematic representation of three different configurations of Schottky defects: (a)  $\langle 100 \rangle$ , (b)  $\langle 110 \rangle$ , and (c)  $\langle 111 \rangle$ . Grey spheres stand for vacancies.

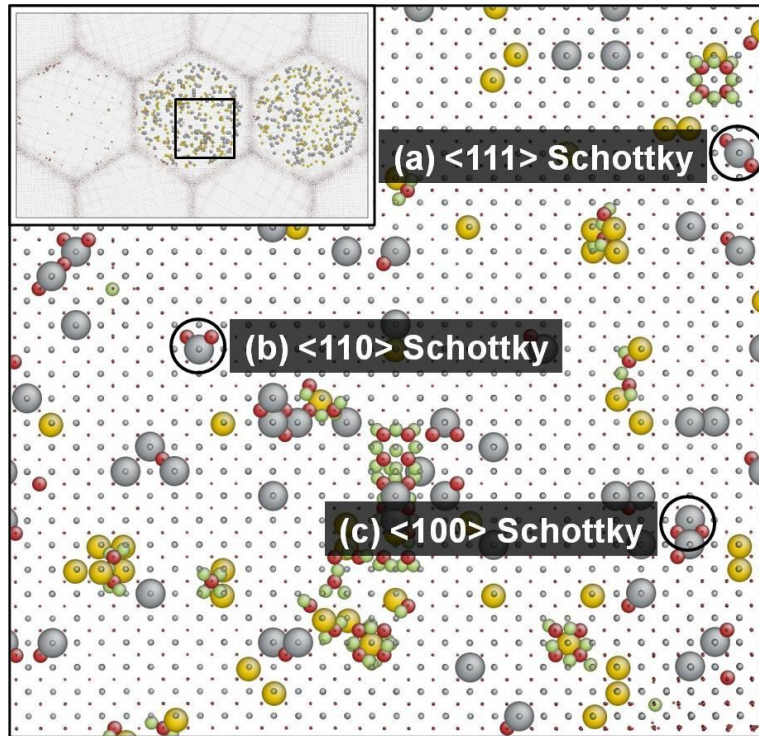


Figure 4-15. Snapshot of selective area showing Schottky defects taken at  $t = 250$  ps: (a)  $\langle 111 \rangle$  Schottky, (b)  $\langle 110 \rangle$  Schottky, and (c)  $\langle 100 \rangle$  Schottky.

vacancies.<sup>88</sup> Hence, even though the Schottky defect is created by diffusion, it is relatively stable. According to the relative positions of the two oxygen vacancies, there are three types of Schottky defects (Fig. 4-14),  $\langle 100 \rangle$ ,  $\langle 110 \rangle$ , and  $\langle 111 \rangle$  Schottky, namely, among which  $\langle 110 \rangle$  and  $\langle 111 \rangle$  Schottky clusters are also observed by Aidhy *et al.* in the single-crystal  $\text{UO}_2$ . In this work<sup>24,37</sup>,  $\langle 100 \rangle$  Schottky is also observed. Three kinds of Schottky defects are simultaneously shown in Fig. 4-15 taken at 250 ps. The formation of the Schottky defect anchors O vacancies, which sequesters them from the vacancy-interstitial recombination. As a result, this leads to their many counterpart O interstitials developing other stable complex clusters.

#### 4.3.5 Interstitial Clustering: Cuboctahedral Clusters

The presence of Schottky defects sequesters O vacancies from their counterparts, so these interstitials develop a relatively complex structure, namely, cuboctahedral

(COT) clusters. Discussion about COT clusters has been well described by Aidhy *et al.* in the work of single-crystal  $\text{UO}_2$ .<sup>24,37</sup> The progressive formation process is recalled in Fig. 4-16. The relative energy is decreasing step by step, indicating that the system tends to form clusters. There are three types of COT clusters defined by the occupancy of the octahedral site (green circle). It can be a U interstitial (COT-*u*), an O interstitial (COT-*o*), or a vacancy (COT-*v*). In this work, three kinds of COT clusters are simultaneously shown in the snapshot taken at 250 ps (Fig 4-17). In addition to COT clusters (a) and (b) already in complete shape, COT clusters (c) and (d) are found to be still under construction, which are found to correspond to the step (c) and (d) in Fig. 4-16. Hence,

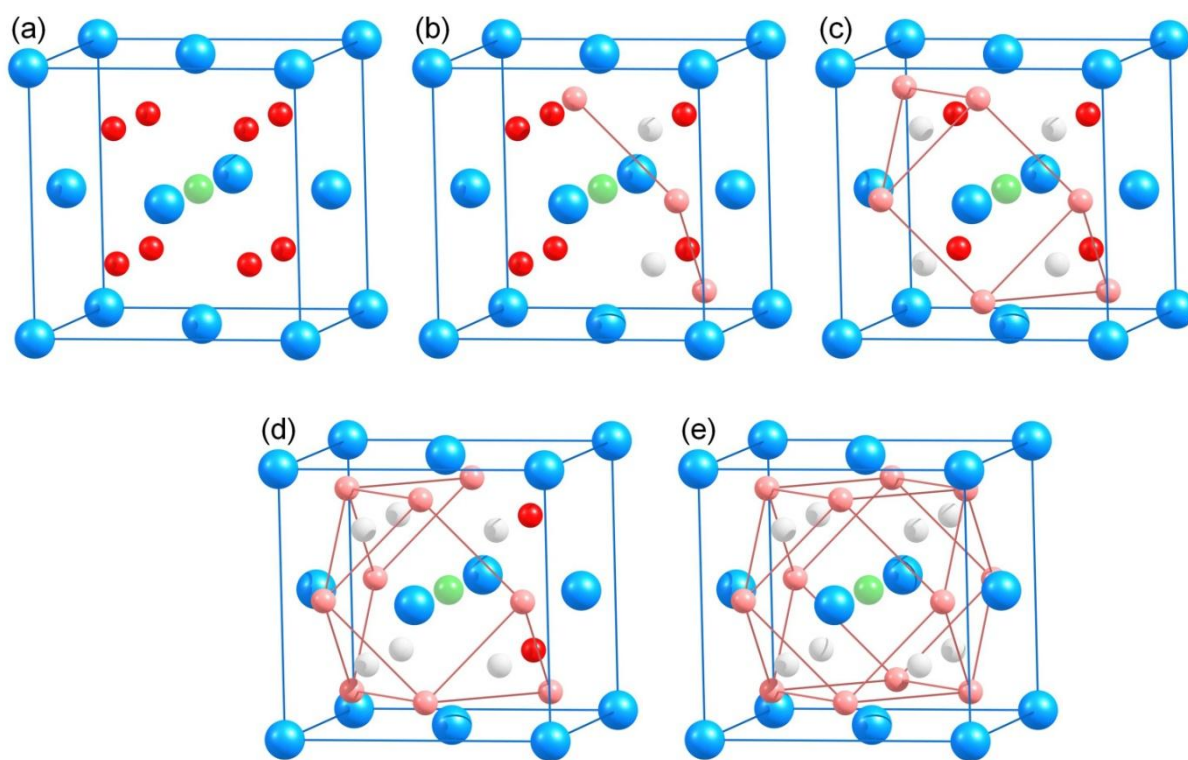


Figure 4-16. Schematic representations of the formation process of COT clusters (blue for U, red for O, pink for O interstitial, grey for O vacancy, and green for either U, O, or vacancy). (a) Fluorite unit cell. (b) The first O interstitial enters the unit cell by knocking two O ions off their original lattice sites, leading to the formation of two vacancies and three interstitials. (c), (d), and (e) are snapshots for the second, third, and fourth O interstitials coming into the unit cell.

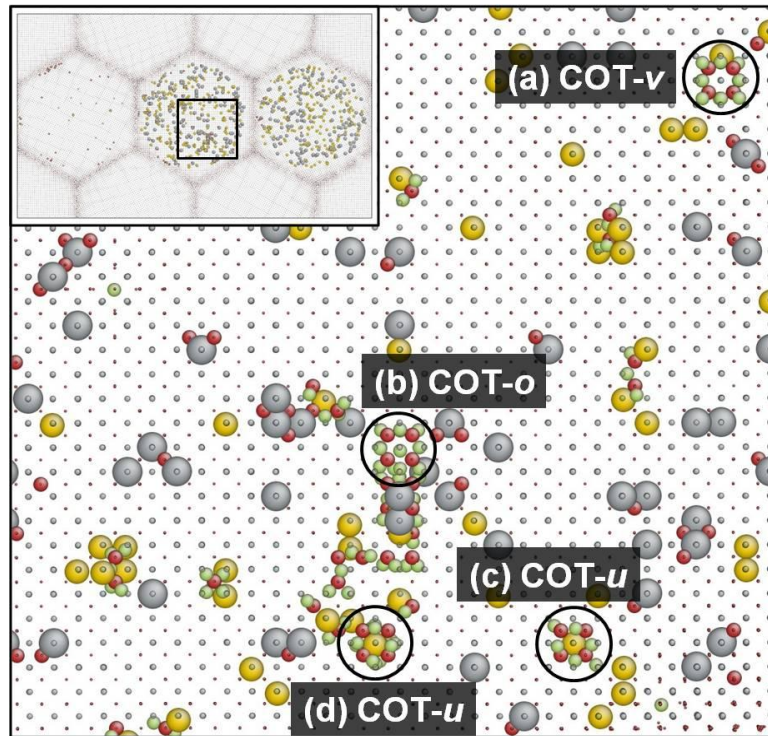


Figure 4-17. Snapshot of selective area showing COT clusters taken at  $t = 250$  ps: (a) COT- $v$ , (b) COT- $o$ , (c) COT- $u$ , and (d) COT- $u$ . It should be noted that both (COT- $u$ )s are not fully constructed.

with the complex structure, the aggregation of interstitials into COT clusters is ascertained to be a rapid but not one-step process. For every complete COT cluster, eight more O FPs will be introduced to the system. This clustering mechanism accounts for the sharp increase in both cases initially with the presence of U FPs.

#### 4.3.6 Interstitial Clustering: V-4O Clusters

In the V-4O cluster, an O vacancy is surrounded by four O interstitials in a pyramidal fashion (Fig. 4-18). The same kind of oxygen cluster is also reported in relaxation of Willis clusters<sup>89,90</sup> by Geng *et al.* using first-principle calculations in  $\text{UO}_{2+x}$ .<sup>91</sup> According to their results, this kind of cluster is the minority among all defects. In the condition of defects on the O sub-lattice alone, most of the O FPs are healed after 400 ps, but two V-4O clusters form. Therefore, from Fig. 4-6, the number of O interstitials is a

little fewer than the number of O vacancies, and the difference is 6. A snapshot taken at 400 ps is shown in Fig. 4-19.

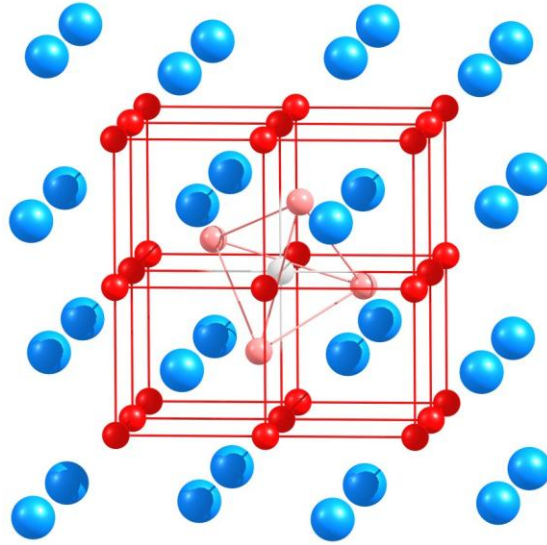


Figure 4-18. Schematic representation of the configurations of V-4O clusters. The O vacancy is surrounded by four O interstitials (grey) in a pyramidal fashion.

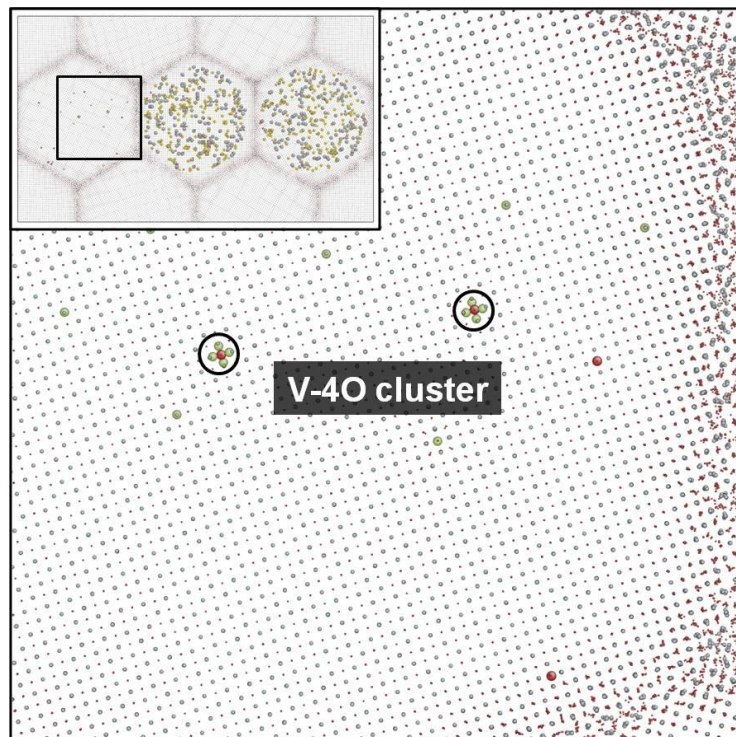


Figure 4-19. Snapshot of selective area showing V-4O oxygen clusters taken at  $t = 400$  ps. In each cluster, an O vacancy is surrounded by four tetrahedral-sited O interstitials.

## CHAPTER 5 CONCLUSIONS AND FUTURE WORK

### 5.1 Conclusions

In terms of analysis tools, the lattice matching analysis (LMA) method is complementary to the conventional common neighbor analysis (CNA) method. The cutoff radius of  $0.19a_o$  (about  $1.039 \text{ \AA}$ ) is tested in the single crystal to identify the same amount and spot of defects as the CNA. The LMA is then applied to polycrystal to determine the exact number, type, and position of every point defect. A big advantage is that it can easily tell the cluster structure.

As for MD simulations, evolution of the defects basically has the same trend as in the single crystal. Similarly, U FPs are seldom annihilated during equilibration while O FPs are mostly healed except those which form clusters. Three kinds of initial conditions are performed. For FPs created on the O sub-lattice alone, the number of O interstitials is slightly larger than that of O vacancies because some charged pyramidal clusters form, in which an O vacancy is surrounded by four O interstitials. In cases of FPs created on the U sub-lattice alone and on both U and O sub-lattices, the number of O vacancies is larger than that of O interstitials. In addition to spontaneous vacancy-interstitial recombination events, point defects have another choice, either diffusing into or emitting from the highly energetic GB. When some of the defects form clusters, one grain bulk region may lose its local electroneutrality. Therefore, GBs maintain the local charge neutrality in the bulk by modulating the defect concentration via source/sink behaviors of point defects. Nevertheless, GBs can be the source and sink for vacancies but only the sink for interstitials. It has been reported by a radiation damage research in copper that formation energy of interstitials at the GB is smaller than in the bulk.<sup>93</sup> Therefore, in  $\text{UO}_2$ ,

the formation energy of oxygen interstitials at the GB can also be smaller than in the bulk. Thus, there is a barrier for interstitials to re-enter the perfect bulk. As a result, no interstitials will be emitted from GBs. In addition, for the case of creating defects on only the U sub-lattice, the equilibrium concentration of O defects is much larger in the polycrystal than that in the single crystal. This can also be explained by the source/sink behaviors with GBs. In the single crystal, the concentration of newly nucleated O defects solely depends on the number of the U FPs. However, in the polycrystal, more O defects can be possibly provided by GBs. Once they successfully enter the interior grain, they will be trapped by forming clusters, such as Schottky or cuboctahedral (COT) clusters.

With respect to the diffusion mechanism, these source/sink activities take place with a set of chain reactions via the vacancy and interstitialcy diffusion. That is, not always the same single atom is moving; instead, many atoms are involved in one diffusion event. The equilibration process is diffusion-controlled, which highly depends on the formation and migration energies of the defects. The diffusion path is ascertained to follow the primary diffusion direction  $\langle 001 \rangle$  for the fluorite-based structure with the reasonable oxygen vacancy diffusion distance.<sup>87</sup> The arrangement of atoms is focused in close-up views to become disordered when the diffusion activity is about to occur; subsequently, all the atoms come back to lattice sites and realign in the normal fashion. In addition, the single point alignment offsets give further quantitative analysis to confirm the phenomena being observed.

Regarding clusters, there are many kinds of clusters formed during equilibration. First, a minor kind of cluster, V-4O, is observed, and the appearance of V-4O clusters accounts for the number of O interstitials is fewer than the number of O vacancies in the

condition of defects on the O sub-lattice alone. Compared with V-4O clusters, Schottky defects and COT clusters are much more prevalent. Schottky defects can be divided into three types by the relative positions of oxygen vacancies:  $\langle 100 \rangle$ ,  $\langle 110 \rangle$ , and  $\langle 111 \rangle$  Schottky. Among them,  $\langle 111 \rangle$  Schottky has the lowest formation energy, followed by  $\langle 110 \rangle$ , and then  $\langle 100 \rangle$  with the Basak potential.<sup>83</sup> Therefore,  $\langle 111 \rangle$  Schottky is the most common type in our simulations. As for COT clusters, there are also three kinds defined by what occupies the octahedral site: COT-*v*, COT-*u*, and COT-*o*. In literature, COT-*o* has lower formation energy than COT-*v*, both negative;<sup>93</sup> nevertheless, there is no information about COT-*u*. Our results show that COT-*u* is the most common. This may be due to the initial high concentration of defects on the U-sub-lattice. Therefore, it can be expected that the formation energy of COT-*u* will be the lowest among these three clusters.

In conclusion, the diffusion-controlled kinetic evolution of defects method is complementary to conventional collision cascade simulations to provide a better understanding of the kinetic phase of defects evolution at the atomistic scale. Extending from the work on the single crystal, this work focuses on the more representative polycrystalline UO<sub>2</sub>. Differences in the numbers of radiation-induced point defects (vacancies and interstitials) are attributed to the presence of GBs, which can modulate the defect concentration via source/sink behaviors. These activities involving the vacancy and interstitialcy diffusion mechanism are evidentially witnessed by atomistic-scale snapshots, along with three types of clusters, V-4O clusters, Schottky defects, and COT clusters. However, with the presence of GBs, whether the radiation tolerance can be enhanced or not is still not determined.

## 5.2 Future Work

This study has been performed on polycrystalline  $\text{UO}_2$  elucidating qualitative GB source/sink strengths. A corresponding work is required to provide more quantitative information. For example, calculating the total number of clusters is needed to identify if GBs essentially enhance or impede the formation of clusters. Actually, GBs open up the possibility of variety of mechanisms that are still not well understood, such as (1) diffusivities in the bulk and GB regions, (2) diffusivities in high- and low-angle misorientation. An understanding of differences of diffusivities in these cases allows us to precisely predict the defect evolution.

## LIST OF REFERENCES

- <sup>1</sup> International Energy Agency (IEA), “Key World Energy Statistics” (2009). ([http://www.iea.org/textbase/nppdf/free/2009/key\\_stats\\_2009.pdf](http://www.iea.org/textbase/nppdf/free/2009/key_stats_2009.pdf)).
- <sup>2</sup> V. S. Arunachalam and E. L. Fleischer, *MRS Bulletin* **33**, 264 (2008).
- <sup>3</sup> E. Rutherford, *Nobel Lecture, Chemistry, 1901-1921 (1908)* (Elsevier, Amsterdam, 1966).
- <sup>4</sup> E. Rutherford, *Radioactivity* in *The Encyclopedia Britannica*, 11<sup>th</sup> edition (Encyclopedia Britannica, New York, 1910).
- <sup>5</sup> U.S. Department of Energy, “The History of Nuclear Energy” (1994). (<http://www.ne.doe.gov/pdfFiles/History.pdf>).
- <sup>6</sup> [http://en.wikipedia.org/wiki/Obninsk\\_Nuclear\\_Power\\_Plant](http://en.wikipedia.org/wiki/Obninsk_Nuclear_Power_Plant).
- <sup>7</sup> [http://en.wikipedia.org/wiki/Nuclear\\_power#Development](http://en.wikipedia.org/wiki/Nuclear_power#Development).
- <sup>8</sup> International Atomic Energy Agency (IAEA), “50 Years of Nuclear Energy”. ([http://www.iaea.org/About/Policy/GC/GC48/Documents/gc48inf-4\\_ftn3.pdf](http://www.iaea.org/About/Policy/GC/GC48/Documents/gc48inf-4_ftn3.pdf)).
- <sup>9</sup> V. S. Arunachalam and E. L. Fleischer, *MRS Bulletin* **33**, 261 (2008).
- <sup>10</sup> B. L. Cohen, *American Journal of Physics* **51**, 75 (1983).
- <sup>11</sup> International Panel on Fissile Materials, “Research Report 8” (2010). (<http://www.ipfmlibrary.org/rr08.pdf>).
- <sup>12</sup> U.S. Energy Information Administration (EIA), U.S. Department of Energy, “Monthly Energy Review” (2010). (<http://www.eia.doe.gov/iea/elec.html>).
- <sup>13</sup> I. Palongengi and K. Kosiński, World Nuclear Association (2009). ([http://en.wikipedia.org/wiki/File:Nuclear\\_power\\_station.svg](http://en.wikipedia.org/wiki/File:Nuclear_power_station.svg)).
- <sup>14</sup> U.S. Energy Information Administration (EIA), U.S. Department of Energy, “World Net Nuclear Reactors”. ([http://www.eia.doe.gov/cneaf/nuclear/page/nuc\\_reactors/reactsum2b.html](http://www.eia.doe.gov/cneaf/nuclear/page/nuc_reactors/reactsum2b.html))
- <sup>15</sup> U.S. Nuclear Regulatory Commission (NRC), “Radioactive Waste: Production, Storage, Disposal” (2002) (<http://www.nrc.gov/reading-rm/doc-collections/nuregs/brochures/br0216/r2/br0216r2.pdf>).
- <sup>16</sup> Movement Against Uranium Mining (MAUM) public education sheet, “Uranium- the Key Element” (<http://www.reachingcriticalwill.org/resources/edkit/22urakey.pdf>).
- <sup>17</sup> H. Becquerel, *Nobel Lecture, Physics 1901-1921 (1903)* (Elsevier, Amsterdam, 1967).

- <sup>18</sup> J. A. Suchocki, *Conceptual Chemistry* (Pearson Benjamin Cummings, San Francisco, 2007).
- <sup>19</sup> J. A. Angelo, *Nuclear Technology* (Greenwood Press, Connecticut, 2004).
- <sup>20</sup> M. Defranceschi and G. Berthier, *Journal of Nuclear Material* **304**, 212 (2002).
- <sup>21</sup> D. Bodansky, *Nuclear Energy – Principles, Practices, and Prospects* (Springer, New York, 2004).
- <sup>22</sup> E. Segrè, *Nuclei and Particles*, 2<sup>nd</sup> edition (McGraw-Hill, New York, 1977).
- <sup>23</sup> F. Ambe, Y. Ohkubo, S. Ambe, Y. Kobayashi, T. Okada, Y. Yanagida, J. Nakamura, K. Asai, Y. Kawase, and S. Uehara, *Journal of Radioanalytical and Nuclear Chemistry* **190**, 215 (1995).
- <sup>24</sup> D. S. Aidhy, P. C. Millett, T. Desai, D. Wolf, and S. R. Phillpot, *Physical Review B* **80**, 104107 (2009).
- <sup>25</sup> B. P. Uberuaga, R. Smith, A. R. Cleave, G. Henkelman, R. W. Grimes, A. F. Voter, and K. E. Sickafus, *Physical Review B* **71**, 104102 (2005).
- <sup>26</sup> P. Pichler, *Intrinsic Point Defects, Impurities and Their Diffusion in Silicon* (Springer-Verlag/Wien, New York, 2004).
- <sup>27</sup> D. R. Askeland and P. P. Phulé, *The Science and Engineering of Materials* (Thomson, 2006).
- <sup>28</sup> V. Y. Freckel, “Yakov Lich Frenkel: his work, life, and letters” (Birkhäuser, Basel Boston Berlin, 1966).
- <sup>29</sup> W. D. Callister, *Materials Science and Engineering: An Introduction*, 7<sup>th</sup> edition (John Wiley & Sons, New York, 2007).
- <sup>30</sup> M. Winning and A. D. Rollett, *Acta Materialia* **53**, 2901 (2005).
- <sup>31</sup> H. Mehrer, *Diffusion in Solids, Fundamentals, Methods, Materials, Diffusion-Controlled Processes* (Springer Berlin Heidelberg, New York, 2007).
- <sup>32</sup> M. W. Barsoum, *Fundamentals of Ceramics*, (Taylor & Francis, New York, 2003).
- <sup>33</sup> J. F. Ziegler, J. P. Biersack, and U. Littmark, *The Stopping and Range of Ions in Matter* (Pergamon, Oxford, 1985).
- <sup>34</sup> M. Nastasi and J. W. Mayer, *Ion Implantation and Synthesis of Materials* (Springer Berlin Heidelberg, New York, 2006).
- <sup>35</sup> M. Bénérière, M. Chemla, and F. Bénérière, *Journal of Applied Physics* **40**, 729 (1979).

- <sup>36</sup> T. Hahn, *International Tables for Crystallography Volume A* (Springer, Fifth Edition, Boston, 2002).
- <sup>37</sup> D. S. Aidhy, Evolution of Intrinsic Point Defects in Fluorite-based Materials: Insights from atomic-level simulation (Dissertation, University of Florida, 2009).
- <sup>38</sup> W. Evans, *Handbook of Materials Modeling*, Edited by S. Yip, 1753 (Springer, Netherlands, 2005).
- <sup>39</sup> L. Q. Chen, *Annual Reviews of Materials Research* **32**, 113 (2002).
- <sup>40</sup> J. D. Gale, *Handbook of Materials Modeling*, Edited by S. Yip, 479 (Springer, Netherlands, 2005).
- <sup>41</sup> A. D. Mackerell, *Handbook of Materials Modeling*, Edited by S. Yip, 509 (Springer, Netherlands, 2005).
- <sup>42</sup> C. J. Cramer, *Essentials of Computational Chemistry Theories and Models*, 2<sup>nd</sup> edition (John Wiley & Sons, West Sussex, 2004).
- <sup>43</sup> L. Verlet, *Physical Review* **159**, 98 (1967).
- <sup>44</sup> R. W. Hockney, *Methods in Computational Physics* **9**, 136 (1970).
- <sup>45</sup> D. Potter, *Computational Physics* (Wiley, New York, 1972).
- <sup>46</sup> D. Beeman, *Journal of Computational Physics* **20**, 130 (1976).
- <sup>47</sup> C. Gear, *Numerical Initial Value Problems in Ordinary Differential Equation* (Prentice-Hall, Englewood Cliffs, NJ, 1971).
- <sup>48</sup> M. P. Allen and D. J. Tildesley, *Computer Simulation of Liquids* (Oxford University Press, Oxford, 1987).
- <sup>49</sup> J. Li, *Handbook of Materials Modeling*, Edited by S. Yip, 565 (Springer, Netherlands, 2005).
- <sup>50</sup> P. P. Ewald, *Annalen der Physik* **64**, 253 (1921).
- <sup>51</sup> R. W. Hockney and J. W. Eastwood, *Computer Simulation Using Particles* (Institute of Physics, Bristol, 1988).
- <sup>52</sup> B. A. Luty, I. G. Tironi, and W. F. van Gunsteren, *Journal of Chemical Physics* **103**, 3014 (1995).
- <sup>53</sup> C. A. White and M. Head-Gordon, *Journal of Chemical Physics* **101**, 6593 (1994).

- <sup>54</sup> M. Challacombe, C. White, and M. Head-Gordon, *Journal of Chemical Physics* **107**, 10131 (1997).
- <sup>55</sup> H. Y. Wang and R. LeSar, *Journal of Chemical Physics* **104**, 4173 (1996).
- <sup>56</sup> A. Y. Toukmaji and J. A. Board Jr., *Computer Physics Communications* **95**, 73 (1996).
- <sup>57</sup> T. Darden, D. York, and L. Pedersen, *Journal of Chemical Physics* **98**, 10089 (1993).
- <sup>58</sup> H. G. Petersen, *Journal of Chemical Physics* **103**, 3668 (1995).
- <sup>59</sup> L. Greengard, *Science* **265**, 909 (1994).
- <sup>60</sup> D. Wolf, P. Keblinski, S. R. Phillpot, J. Eggebrecht, *Journal of Chemical Physics* **110**, 8254 (1999).
- <sup>61</sup> D. Wolf, *Physical Review Letters* **62**, 3315 (1992).
- <sup>62</sup> F. Ruhr, K. Wirth, J. Libuda, D. Capptus, M. Bäumer, and H.-J. Freund, *Surface Science* **315**, L977 (1994).
- <sup>63</sup> Y. Ida, *Physics of the Earth Planetary Interiors* **13**, 97 (1976).
- <sup>64</sup> C. B. Basak, A. K. Sengupta, and H. Kamath, *Journal of Alloys and Compounds* **360**, 210 (2003).
- <sup>65</sup> S. Nosé, *Molecular Physics* **52**, 255 (1984).
- <sup>66</sup> S. Nosé, *Journal of Chemical Physics* **81**, 511 (1984).
- <sup>67</sup> H. J. C. Berendsen, J. P. M. Postma, and W. F. Vangunsteren, *Journal of Chemical Physics* **81**, 3684 (1984).
- <sup>68</sup> S. A. Adelman, J. D. Doll, *Journal of Chemical Physics* **64**, 2375 (1976).
- <sup>69</sup> H. C. Andersen, *Journal of Chemical Physics* **72**, 2384 (1977).
- <sup>70</sup> M. Parrinello and A. Rahman, *Physical Review Letters* **45**, 1196 (1980).
- <sup>71</sup> M. Parrinello and A. Rahman, *Journal of Chemical Physics* **76**, 2662 (1982).
- <sup>72</sup> M. T. Robinson and I. M. Torrens, *Physical Review B* **9**, 5008 (1974).
- <sup>73</sup> R. Stoller, *Journal of Materials-Journal of Minerals Metals and Materials Society* **48**, 23 (1996).
- <sup>74</sup> T. D. de la Rubia, H. M. Zbib, T. A. Kharaiishi, B. D. Wirth, M. Victoria, and M. J. Caturla, *Nature* **406**, 24 (2000).

- <sup>75</sup> B.P. Uberuaga, R. Smith, A.R. Cleave, F. Montalenti, G. Henkelman, R.W. Grimes, A.F. Voter, and K.E. Sickafus, *Physical Review Letters* **92**, 115505 (2004).
- <sup>76</sup> Y. Matsukawa and S.J. Zinkle, *Science* **318**, 959 (2007).
- <sup>77</sup> B.P. Uberuaga, R. Smith, A.R. Cleave, F. Montalenti, G. Henkelman, R.W. Grimes, A.F. Voter, and K.E. Sickafus, *Physical Review Letters* **92**, 115505 (2004).
- <sup>78</sup> B.P. Uberuaga, R. Smith, A.R. Cleave, G. Henkelman, R.W. Grimes, A.F. Voter, and K.E. Sickafus, *Physical Review B* **71**, 104102 (2005).
- <sup>79</sup> T. G. Desai, P. C. Millett, and D. Wolf, *Acta Materialia* **56**, 4489 (2008).
- <sup>80</sup> J. P. Hiernaut, G. J. Hyland, and C. Ronchi, *International Journal of Thermophysics* **14**, 259 (1993).
- <sup>81</sup> J. Ralph, *J. Chem. Soc., Faraday Transactions II* **87**, 1253 (1987).
- <sup>82</sup> J. D. Honeycutt and H. C. Andersen, *Journal of Physical Chemistry* **91**, 4950 (1987).
- <sup>83</sup> K. Govers, S. Lemehov, M. Hou, and M. Verwerft, *Journal of Nuclear Materials* **366**, 161 (2007).
- <sup>84</sup> A. P. Sutton and R. W. Balluffi, *Interfaces in Crystalline Materials* (Clarendon Press, Oxford, 1995).
- <sup>85</sup> P. C. Millett, D. S. Aidhy, T. Desai, S. R. Phillpot, D. Wolf, *International Journal of Materials Research* **100**, 550 (2009).
- <sup>86</sup> K. Govers, S. Lemehov, M. Hou, and M. Verwerft, *Journal of Nuclear Materials* **395**, 131 (2009).
- <sup>87</sup> D. S. Aidhy, S. B. Sinnott, E. D. Wachsman, and S. R. Phillpot, *Ionics* **16**, 297 (2010).
- <sup>88</sup> R. A. Jackson, and C. R. A. Catlow, *Journal of Nuclear Materials* **127**, 161 (1985).
- <sup>89</sup> B. T. M. Willis, *Proceedings of the British Ceramic Society* **1**, 9 (1964).
- <sup>90</sup> B. T. M. Willis, *Acta Crystallography, Section A: Crystal Physics, Diffraction, Theoretical and General Crystallography* **A34**, 88 (1978).
- <sup>91</sup> H. Y. Geng, Y. Chen, Y. Kaneta, and M. Kinoshita, *Applied Physics Letters* **93**, 201903 (2008).
- <sup>92</sup> X.-M. Bai, A. F. Voter, R. G. Hoagland, M. Nastasi, and B. P. Uberuaga, *Science* **327**, 1631 (2010).
- <sup>93</sup> H. Y. Geng, Y. Chen, and Y. Kaneta, *Physical Review B* **77**, 180101 (2008).

## BIOGRAPHICAL SKETCH

Kun-Ta Tsai was born in Hsinchu, Taiwan. He received his bachelor's degree in chemical engineering from National Cheng-Kung University, Tainan, Taiwan, in 2007.

Kun-Ta came to the United States to pursue higher education and entered the Department of Materials Science and Engineering at University of Florida, Gainesville, in Fall 2008. He joined the Computational Materials Science Focus Group with Prof. Simon R. Phillpot in Spring 2009. Kun-Ta is expecting his master's degree in Summer 2010.

After joining the Gator Nation, Kun-Ta watched his first football game in his life, and started to become crazy about it. In the same academic year, the Florida Gators won the Bowl Championship Series (BCS) National Championships. He is proud to say "Go Gators".